Thermal Science and Engineering Progress 49 (2024) 102497

Contents lists available at ScienceDirect

Thermal Science and Engineering Progress

journal homepage: www.elsevier.com/locate/tsep

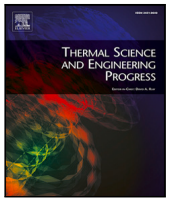

Integrating artificial intelligence in investigating magneto-bioconvection flow of oxytactic microorganisms and nano-enhanced phase change material in H-type cavity

Shafqat Hussain [a,*], Abdelraheem M. Aly [b], Noura Alsedias [c], Andaç Batur Çolak [d]

[a] Institut für Angewandte Mathematik (LS III), Fakultät für Mathematik, Technische Universität Dortmund, 44227 Dortmund, Germany
[b] Department of Mathematics, College of Science, King Khalid University, Saudi Arabia
[c] Department of Mathematical Sciences, College of Science, Princess Nourah bint Abdulrahman University, P.O. Box 84428, Riyadh 11671, Saudi Arabia
[d] IT Application and Research Center, Istanbul Ticaret University, Türkiye

ARTICLE INFO

Keywords:
Nanoparticle-enhanced phase change materials
Galerkin FEM
H-shaped porous cavity
Artificial intelligence
Inclined magnetic field
Oxytactic bacteria

ABSTRACT

Nano-enhanced phase change materials is an effective way to improve the thermal characteristics and to minimize energy consumption. The bioconvection flow of nano-enhanced phase change materials is gaining more attention in recent investigations due to its significant applications in engineering and medical sciences. The present study aims to numerically explore magneto-bioconvection flow of nano-enhanced phase change materials in H-type cavity including oxytactic microorganisms. The cavity is constantly heated from the left and a right wall is maintained at cold temperature. The major focus of the current investigation is analyzing the flow and thermal features of the suspension of nano-enhanced phase change materials and a host fluid. The governing system is reduced to the dimensionless form by applying the appropriate transformation. Impact of pertinent parameters, porosity, cavity aspect ratio, Darcy, Hartmann, Lewis, Rayleigh, bioconvection Rayleigh numbers, radiation parameter, and Péclet number on bioconvection flow of oxytactic microorganisms in H-type cavity has been analyzed. Six various artificial neural network models are explored in order to estimate critical parameters with an artificial intelligence approach. It is found that the variations of a cavity aspect ratio are enhancing the bioconvection flow and phase change material. Increasing Hartmann number reduces the nanofluid velocity and distributions of oxygen and microorganisms. The Rayleigh and bioconvection Rayleigh numbers are playing an importance role in enhancing bioconvection flow and varying phase change material.As Ha increases from 10 to 100, at $\gamma = 90^0$, there is a 1.67% decrease in the values of Nu_{avg} and a 0.247% increase in Sh_{avg}. Among the study findings, the developed artificial neural networks can predict each parameter with high accuracy.

1. Introduction

In the recent years, there are several applications of bioconvection flows in biomicrosystems, heat exchangers, fuel cells, biological wastes, and oil recovery, etc., [1–4]. The bioconvection flow is produced by the traveling microorganisms under the influences of an oxygen as a chemical reaction. Additionally, the spare bacteria supports the bioconvection flow since the bacteria is heavier than water. The bioconvection flow investigates spontaneous design formation and mass stratification in the specific situation of direct communication between microbes, forces, and nanoparticles. Many fields and technologies make use of bioconvection, including medicine, biological polymer synthesis, environmental protection, renewable technology, microbial oil recovery, biosensors, and biotechnology. Shen et al. [5] investigated the effects of temperature jump on bioconvection flow of a nanofluid including gyrotactic microorganisms. Zohra et al. [6] investigated the influences of Stefan processing on bioconvection flow of a nanofluid. Nanofluids with magneto-transport phenomena were studied by Rana et al. [7], determining how gyrotactic behavior in an algal suspension affected the flow of the fluid along an expanding cylinder. The research was carried out using Cattaneo-heat Christov's flux and mass flux concepts in a modified Buongiorno model. Nabwe et al. [8] examined Carreau

* Corresponding author.
E-mail address: shafqat.hussain@math.tu-dortmund.de (S. Hussain).

https://doi.org/10.1016/j.tsep.2024.102497
Received 27 November 2023; Received in revised form 21 February 2024; Accepted 29 February 2024
Available online 1 March 2024

Nomenclature

C	oxygen concentration
C_p	specific heat (J kg^{-1} K^{-1})
D_c	oxygen diffusivity, m^2 s^{-1}
D_n	microorganisms diffusivity, m^2 s^{-1}
g	gravitational acceleration (m s^{-2})
H	length (m)
Ha	Hartmann number
h_{sf}	latent heat of the core (KJ kg^{-1})
k	thermal conductivity (W m^{-1} K^{-1})
L	cavity dimension (m)
Le	Lewis number, $\frac{\alpha_f}{D_c}$
m	motile microorganisms (dimensional)
m_0	the reference density number
N	motile microorganisms density
Nu	Nusselt number (local)
Nu_{avg}	Nusselt number (average)
p	pressure, (N m^{-2})
Pe	Peclet number
Pr	Prandtl number, $\frac{\nu_f}{\alpha_f}$
q_r	radiative heat flux
Ra	Rayleigh number
Rb	bioconvection Rayleigh number
Rd	Radiation parameter
Sh	Sherwood number (local),
Sh_{avg}	Sherwood number (average)
Ste	Stefan number
T	temperature (K)
T_{Mr}	melting temperature range
u, v	velocities (m s^{-1})
x, y	Cartesian coordinates (m)
X, Y	dimensionless Cartesian coordinates

Abbreviations

MSE	Mean squared error
MLP	Multilayer perceptron
ANN	Artificial neural network
MoD	Margin of deviation
R	Coefficient of determination
AR	Cavity aspect ratio

Greek symbols

α	thermal-diffusivity (m^2 s^{-1})
β	thermal expansion coefficient (K^{-1})
γ	angle of magnetic field
ϵ	porosity
η	mass ratio of core to the shell
θ	dimensionless temperature
μ	dynamic-viscosity (kg m^{-1}s^{-1})
ν	kinematic-viscosity (m^2 s^{-1})
ξ	oxygen concentration
ρ	density (kg m^{-3})
ϕ	nanoparticles concentration
ψ	stream function

Subscripts

avg	average
b	bulk properties of the suspension
co	properties of the core of NEPCM particle
c	cold
f	water properties
h	hot
p	nanoparticle containing PCM
s	solid
sh	properties of the shell of NEPCM particle
w	wall

nanofluid and swimming gyrotactic microorganisms over an angled stretchable cylinder. Hussain et al. [9] investigated bioconvection flow of a hybrid nanofluid with an obstruction, and oxytactic bacteria within a porous enclosure.

The industrial system is reliant on a base fluid that is insufficient to meet the requirements of industrial processes. To address this issue, a new phase of nanotechnology is proposed to assist them in achieving their goals. Nanofluids can be used in machines to improve refrigeration and air conditioning, as well as for cooling and shock absorption. Guided by these applications, several researchers investigated the flow of nanoliquids past various surfaces. Choi and Eastman [10] was the first to demonstrate an innovative method of increasing thermal conductivity using nanofluid and, thus, heat transfer performance of industrial systems. An unusual property of nanofluids is the increased heat transfer rates that result from their exceptionally high thermal conductivity compared to that of conventional fluids. Numerous scientists have investigated the peculiar behaviors of nanofluids, and numerous metallic nanoparticles have been examined [11–13]. Mebarek et al. [14] investigated the influences of five different thermal sources on convection of nanofluids in two coaxial cylindrical tubes using the finite volume technique. Ahlawat and Sharma [15] investigated the effects of heated block and porous stratum on heat convection inside a micropolar hybrid nanofluid-occupied an enclosure.

The bioconvection flow of the nanofluid and oxytactic microorganisms are introduced in [16–18]. The water's density is increasing by swimming of the motile microorganisms. Das et al. [18] presented hydromagnetic bioconvection of nanofluid with gyrotactic microorganisms over a porous plate. Oreyeni et al. [19] investigated the impact of MHD heat, and mass transfer, along with the behavior of gyrotactic microorganisms, on the flow of bioconvective micropolar nanofluid over a stretched surface subject to triple stratifications and Cattaneo–Christov double diffusion. Shamshuddin et al. [20] concentrate on applying bioconvective treatment to study the flow of a reactive Casson hybrid nanofluid past an exponentially stretching sheet under the influence of Ohmic heating and mixed convection.

Many problems in fluid dynamics have been solved using Boussinesq approximations, with most cases having successful results compared to experiments. Mastiani et al. [21] investigated the mixed convection within a lid-driven enclosure. Vasu et al. [22] presented a theoretical work using the nonlinear Boussinesq approximation for transient mixed convection of a nanofluid. Asmadi et al. [23] used Boussinesq approximation for natural convection inside a nanofluid-occupied U-shaped enclosure. Ramesh et al. [24] employed mathematical modeling to analyze nanofluid behavior in the presence of electro-magnetohydrodynamics (EHD) and thermal radiation. They utilize the Jeffrey fluid model to investigate the Graetz problem in a micro-channel, considering lubrication effects. Additionally, the study incorporates Poisson–Boltzmann and Navier–Stokes equations to model electro-osmotic nanofluid flow with a heat sink source.

Due to the uses of NEPCMs in improving heat transfer, many investigations on natural/mixed convection flows of NEPCM inside cavities are performed in [25–28]. The bioconvection flow inside cavities containing oxytactic microorganisms and suspended by NEPCMs is recently introduced by Hussain et al. [29,30]. In this study, the magnetic field

impacts on the bioconvection flow within H-type cavity containing NEPCM and oxytactic microorganisms are studied numerically by using the Galerkin FEM and artificial intelligence approach.

The primary motivation for the present investigation in deepening our understanding of intricate fluid dynamics and heat transfer phenomena within biological and thermal contexts. This interdisciplinary approach employs AI techniques to analyze and enhance the behaviors of microorganisms and nano-enhanced materials a midst fluid dynamics, thereby enabling various specific applications: In Biomedical Engineering, the comprehension of microorganisms' responses to magnetic fields and fluid motion offers potential for the advancement of targeted drug delivery systems or medical interventions reliant on biological fluids. In the realm of Renewable Energy, the exploration of phase change materials' behavior within fluid flows provides insights for designing more efficient thermal energy storage mechanisms for renewable energy solutions like solar power. Within Material Science, the investigation into the interplay between nano-enhanced materials and fluid dynamics propels the development of advanced materials tailored to specific thermal properties, applicable in diverse fields such as aerospace or electronics cooling. Overall, the integration of AI into the exploration of such complex systems promises to reveal unique insights, streamline processes, and stimulate the emergence of innovative technologies with varied practical implications across multiple domains. The selection of an H-type enclosure for study is driven by its practical applicability, adaptable geometry, scalability, and potential for comparative analysis, rendering it an invaluable tool for exploring fluid dynamics and heat transfer in engineering contexts.

2. The physical model

The proposed model consists of H-type cavity as depicted in Fig. 1 saturated with laminar, steady, incompressible, and natural-bio convective flow. The cavity is filled with a water based suspension of nano-encapsulated phase change materials in the presence of oxytactic microorganisms. The cavity side length is denoted by L. The aspect ratio of the cavity is defined as $AR = H/L$, where H is length as demonstrated in the figure. The left wall of the cavity is fixed at constant hot temperature (T_h) while the right wall of the cavity is kept cold at temperature (T_c). All the remaining walls are perfectly insulated. The nano-encapsulated phase-change materials consists of the core and shell as the encapsulation material. The core of NEPCM undergoes a phase transition at the fusion temperature (T_f). During the phase transition to liquid, it absorbs/releases its energy in the form of latent heat, see [31–33] for further details. The proposed problem is further subjected to the following assumptions:

- The phase change nanoparticles are assumed to be well dispersed in the base fluid.
- The magnetic field is imposed to be an inclined with a strength B_0.
- The physical domain is saturated with a stable suspension of nanoparticles.
- The local thermal equilibrium is applied amongst a base fluid and a porous medium.
- Adding nanoparticles is not affecting on the velocity and direction of bacteria's swimming.
- The density variation is accounted using Boussinesq approximation.

Table 1 provides the thermal properties of nanoparticles, base fluid, and a porous medium.

The bulk features of thermo-physical are involved in the controlling PDEs need to be evaluated before solving the obtained model related characteristics of water and NEPCMs, see [33,34] for the utilized thermo-physical properties in the dimensional form.

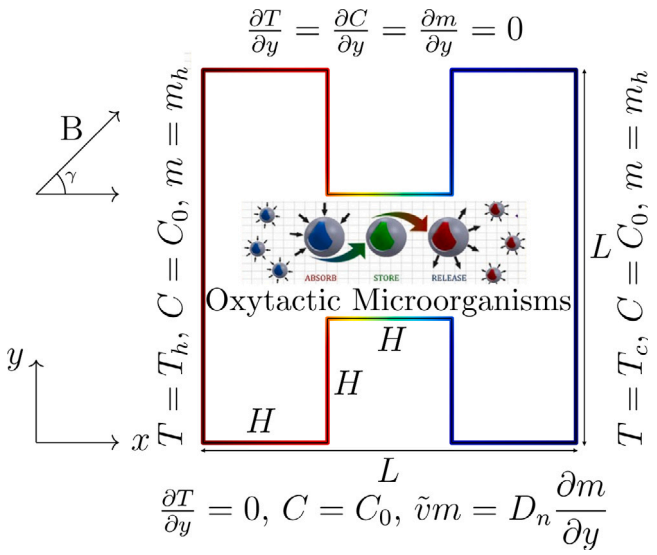

Fig. 1. Problem configuration.

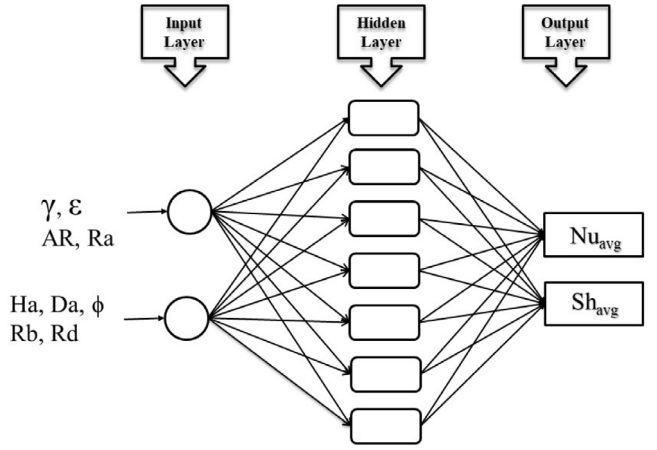

Fig. 2. Architecture of the developed MLP network.

Table 1
Thermal features of NEPCM suspension [32].

	Material	ρ	$\beta \times 10^{-5}$	C_p	k
Host fluid	Water	997.1	21	4179	0.613
Core	Nonadecane	786	17.28	1317.7	– – –
Shell	Polyurethane	721	– – –	2037	– – –
Porous matrix	Glass balls	2700	– – –	840	1.05

The proposed problem is controlled by laws of mass, momentum, energy, oxygen and microorganism conservation [33,34]:

$$\frac{\partial u}{\partial x} + \frac{\partial v}{\partial y} = 0 \tag{1a}$$

$$\frac{\mu_b}{\epsilon}\nabla^2 u = \frac{\partial p}{\partial x} + \frac{\rho_b}{\epsilon^2}\left(u\frac{\partial u}{\partial x} + v\frac{\partial u}{\partial y}\right) + f_x \tag{1b}$$

$$\frac{\mu_b}{\epsilon}\nabla^2 v = \frac{\partial p}{\partial y} + \frac{\rho_b}{\epsilon^2}\left(u\frac{\partial v}{\partial x} + v\frac{\partial v}{\partial y}\right) + f_y \tag{1c}$$

$$\frac{k_{eff}}{(\rho C_P)_b}\nabla^2 T = u\frac{\partial T}{\partial x} + v\frac{\partial T}{\partial y} + \frac{1}{(\rho C_P)_b}\frac{\partial q_r}{\partial y} \tag{1d}$$

$$D_c\nabla^2 C = u\frac{\partial C}{\partial x} + v\frac{\partial C}{\partial y} + \delta m \tag{1e}$$

$$\frac{\partial}{\partial x}\left[um + \tilde{u}m - D_n\frac{\partial m}{\partial x}\right] + \frac{\partial}{\partial y}\left[vm + \tilde{v}m - D_n\frac{\partial m}{\partial y}\right] = 0, \tag{1f}$$

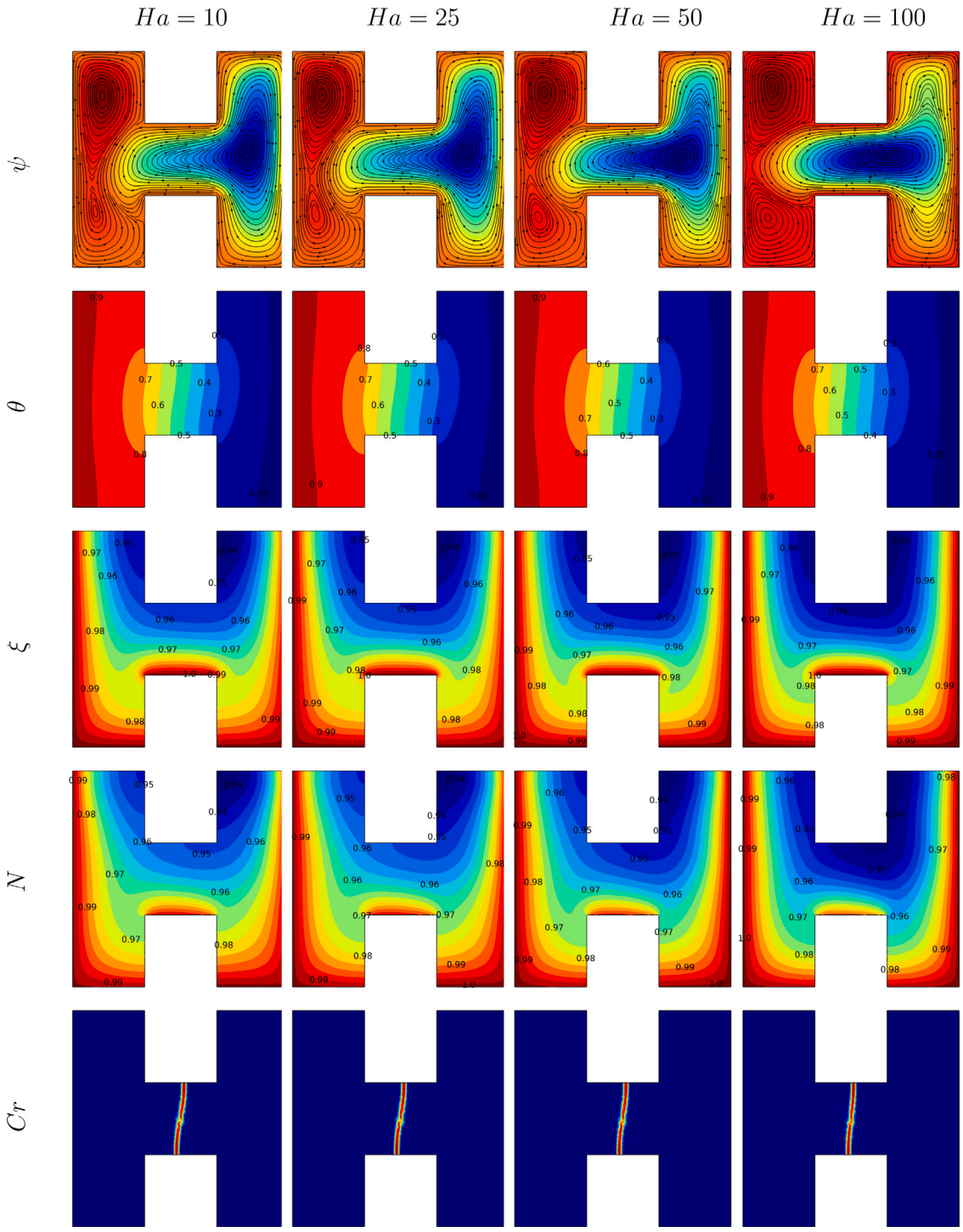

Fig. 3. The contours of ψ, θ, ξ, N, and Cr below the variations of Ha at $Pr = 6.2, Le = Pe = 1, Ra = 10^5, Ste = \theta_f = 0.5, \phi = 0.05, \epsilon = 0.8, \gamma = 0, AR = 1/3, Da = 10^{-3}, Rd = 1, \chi = \zeta = 1$, and $R_b = 10$.

where the body forces are given as

$$f_x = \frac{\mu_b}{K}u + \frac{\rho_b C_f}{\sqrt{K}}u\sqrt{u^2+v^2} + \frac{\sigma_b B_0^2}{\rho_b}\left(v\sin\gamma\cos\gamma - u\sin^2\gamma\right) \tag{2a}$$

$$f_y = \frac{\mu_b}{K}v + \frac{\rho_b C_f}{\sqrt{K}}v\sqrt{u^2+v^2} + \frac{\sigma_b B_0^2}{\rho_b}\left(u\sin\gamma\cos\gamma - v\cos^2\gamma\right) + (\gamma^\star \Delta\rho \cdot m - (\rho\beta)_b(T - T_c))g \tag{2b}$$

where $C_f = 1.75/\sqrt{150\epsilon^3}$ stands for the Forchheimer coefficient, $k_{eff} = (1-\epsilon)k_s + \epsilon k_f$ denotes the effective thermal conductivity, $K = \epsilon^3 d_{ps}^2/150(1-\epsilon)^2$ is the permeability, d_{ps} stands for the average size of particle of a porous matrix, $\tilde{u} = \left(\frac{bW_c}{\Delta C}\right)\frac{\partial C}{\partial x}$ and $\tilde{v} = \left(\frac{bW_c}{\Delta C}\right)\frac{\partial C}{\partial y}$ explains the mean swimming velocities of bacteria. C_0 represents the oxygen concentration for right and left walls, W_c is the maximum cell swimming speed, δm denotes oxygen usage of bacteria, $\gamma^\star$ representing the mean volume of bacteria and $\Delta C = C_0 - C_{\min}$ where $C_{\min}$ is a minimum oxygen concentration. The radiative heat flux is adopted by Rosseland approximation as $q_r = -(4\sigma_B/3\beta_R)(\partial T^4/\partial y)$. Under the assumption of small temperature differences, the temperature T^4 is

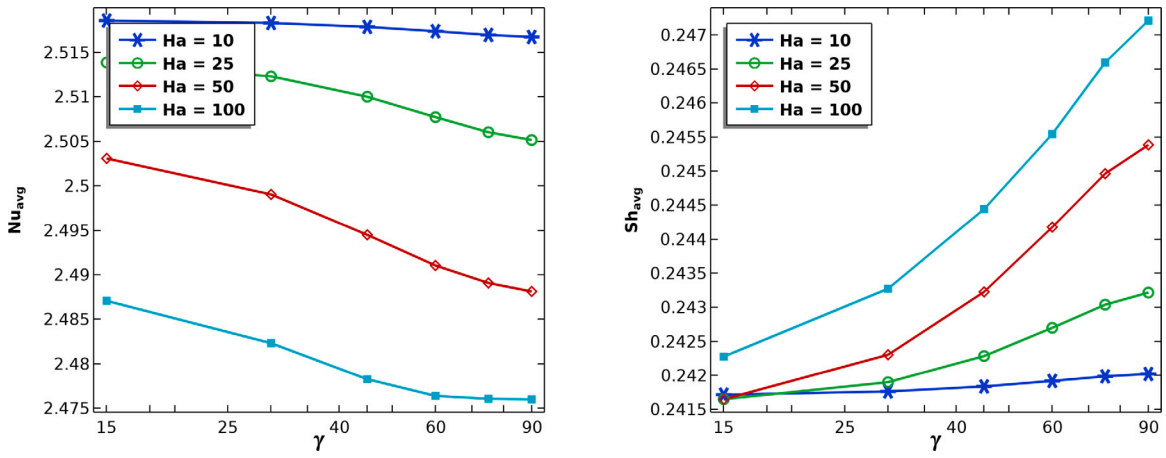

Fig. 4. The Nu_{avg} and Sh_{avg} below the variations of Ha and γ at $AR = 1/3, Pr = 6.2, Ra = 10^5, Da = 10^{-3}, Le = Pe = 1, Ste = \theta_f = 0.5, \epsilon = 0.8, \phi = 0.05, Rd = 1, \chi = \zeta = 1,$ and $R_b = 10$.

approximated on T using the well-known Taylor series expansion.

$$T^4 \approx 4T_c^3 T - 3T_c^4 \tag{3}$$

and

$$\frac{\partial q_r}{\partial y} = -\left(\frac{16\sigma_B T_c^3}{3\beta_R}\right)\frac{\partial^2 T}{\partial y^2}. \tag{4}$$

The dimensional system of Eq. (1) is reduced to the dimensionless form with the following transformations:

$$\begin{aligned} &X = \frac{x}{L}, Y = \frac{y}{L}, U = \frac{uL}{\alpha_f}, V = \frac{vL}{\alpha_f}, \\ &P = \frac{pL^2}{\rho\alpha_f^2}, \theta = \frac{T - T_c}{T_h - T_c}, \xi = \frac{C - C_{\min}}{\Delta C}, N = \frac{m}{m_0}. \end{aligned} \tag{5}$$

Once the dimensionless system of PDEs is achieved with the help of above variables. Thus, the dimensionless system becomes:

$$\frac{\partial U}{\partial X} = -\frac{\partial V}{\partial Y}, \tag{6a}$$

$$Pr(1 + N_v\phi)\nabla^2 U = \frac{\partial P}{\partial X} + \frac{1}{\epsilon^2}\left(\frac{\mu_b}{\rho_f}\right)\left(U\frac{\partial U}{\partial X} + V\frac{\partial U}{\partial Y}\right) + F_X \tag{6b}$$

$$Pr(1 + N_v\phi)\nabla^2 V = \frac{\partial P}{\partial Y} + \frac{1}{\epsilon^2}\left(\frac{\mu_b}{\rho_f}\right)\left(U\frac{\partial V}{\partial X} + V\frac{\partial V}{\partial Y}\right) + F_Y \tag{6c}$$

$$\frac{k_{m,b}}{k_f}\left[\frac{\partial^2\theta}{\partial X^2} + \left(1 + \frac{4Rd}{3}\right)\frac{\partial^2\theta}{\partial Y^2}\right] = Cr\left(U\frac{\partial\theta}{\partial X} + V\frac{\partial\theta}{\partial Y}\right) \tag{6d}$$

$$\frac{1}{Le}\nabla^2\xi = U\frac{\partial\xi}{\partial X} + V\frac{\partial\xi}{\partial Y} + \frac{\zeta}{Le}N \tag{6e}$$

$$\begin{aligned} \frac{1}{Le}\nabla^2 N = {} & \chi\left(U\frac{\partial N}{\partial X} + V\frac{\partial N}{\partial Y}\right) \\ & + \frac{Pe}{Le}\left(N\frac{\partial^2\xi}{\partial X^2} + N\frac{\partial^2\xi}{\partial Y^2} + \frac{\partial N}{\partial X}\frac{\partial\xi}{\partial X} + \frac{\partial N}{\partial Y}\frac{\partial\xi}{\partial Y}\right), \end{aligned} \tag{6f}$$

where

$$F_X = \frac{1}{Da}U + \frac{C_f}{\sqrt{Da\epsilon^3}}U\sqrt{U^2 + V^2} + \left(\frac{\sigma_b}{\sigma_f}\right)\left(\frac{\beta_b}{\beta_f}\right)(V\sin\gamma\cos\gamma - U\sin^2\gamma) \tag{7a}$$

$$\begin{aligned} F_Y = {} & \frac{1}{Da}V + \frac{C_f}{\sqrt{Da\epsilon^3}}V\sqrt{U^2 + V^2} + \left(\frac{\sigma_b}{\sigma_f}\right)\left(\frac{\beta_b}{\beta_f}\right)(U\sin\gamma\cos\gamma - V\cos^2\gamma) \\ & + RaPr\left(\frac{\rho_b}{\rho_f}\right)\left(\frac{\beta_b}{\beta_f}\right)(\theta - R_b N) \end{aligned} \tag{7b}$$

where $\chi = D_c/D_n$ depicts the diffusion ratio and $\zeta = (m_0\delta L^2/(D_c\Delta C))$ denotes the consumption of oxygen. The heat capacity ratio Cr and effective thermal conductivity of a suspension and porous medium $(k_{m,b})$ in (6d) are given by

$$Cr = (\rho C_p)_b/(\rho C_p)_f = (1-\phi) + \phi\xi + \frac{\phi}{\delta Ste}f, \quad \frac{k_{m,b}}{k_f} = (1-\epsilon)\frac{k_s}{k_f} + \epsilon(1 + N_c\phi). \tag{8}$$

The involved parameters in (6) such as Prandtl number, Rayleigh, bioconvection Rayleigh, Hartmann, Peclet, Darcy, Lewis numbers and thermal radiation parameter are given by:

$$Pr = \frac{\nu_f}{\alpha_f}, Ra = \frac{\beta_T g L^3 \Delta T Pr}{\nu^2}, R_b = \frac{m_0(\rho_{cell} - \rho_f)\gamma}{\rho_f\beta_f(T_h - T_c)}, \tag{9a}$$

$$Ha = B_0 L\sqrt{\frac{\sigma_f}{\mu_f}}, Pe = \frac{bW_c}{D_n}, Le = \frac{\alpha_f}{D_c}, Da = \frac{K}{L^2}, Rd = \frac{4\sigma_B T_c^3}{k_f\beta_R}. \tag{9b}$$

The heat capacity ratio (ξ), Stefan number (Ste), and melting temperature interval (δ), are:

$$\begin{aligned} \lambda &= \frac{\left(C_{p,co} + \eta C_{p,sh}\right)\rho_{co}\rho_{sh}}{\left(\rho C_p\right)_f\left(\rho_{sh} + \eta\rho_{co}\right)}, \qquad \delta = \frac{T_{Mr}}{\Delta T}, \\ Ste &= \frac{\Delta T\left(\rho C_p\right)_f\left(\rho_{sh} + \eta\rho_{co}\right)}{h_{sf}\rho_{co}\rho_{sh}(1+\eta)}. \end{aligned} \tag{10}$$

The following is the fusion-function, demonstrated as a function of temperature

$$f = \left\{\frac{\pi}{2}\cdot\sin\left(\frac{\pi}{\delta}\left(\theta - \theta_f + \frac{\pi}{2}\right)\right)\right\}\cdot\begin{cases} 0 & \text{if} \quad \theta < \theta_f - \frac{\delta}{2} \\ 1 & \text{if} \quad \theta_f - \frac{\delta}{2} < \theta < \theta_f + \frac{\delta}{2} \\ 0 & \text{if} \quad \theta > \theta_f + \frac{\delta}{2} \end{cases} \tag{11}$$

where the fusion temperature (θ_f) can be reduced as

$$\theta_f = \frac{T_f - T_c}{T_h - T_c}. \tag{12}$$

The boundary conditions in the dimensionless form are subjected to the no-slip velocity $U = V = 0$. Thermal and concentration components are subjected to the following constraints

On the right wall: $\xi = N = 1, \theta = 0$

On the bottom walls: $\frac{\partial\theta}{\partial Y} = 0, \xi = 1, PeN\frac{\partial\xi}{\partial Y} = \frac{\partial N}{\partial Y}$

On the left wall: $\theta = 1, \xi = N = 1$

On the other walls: $\frac{\partial\theta}{\partial Y} = \frac{\partial\xi}{\partial Y} = \frac{\partial N}{\partial Y} = 0.$

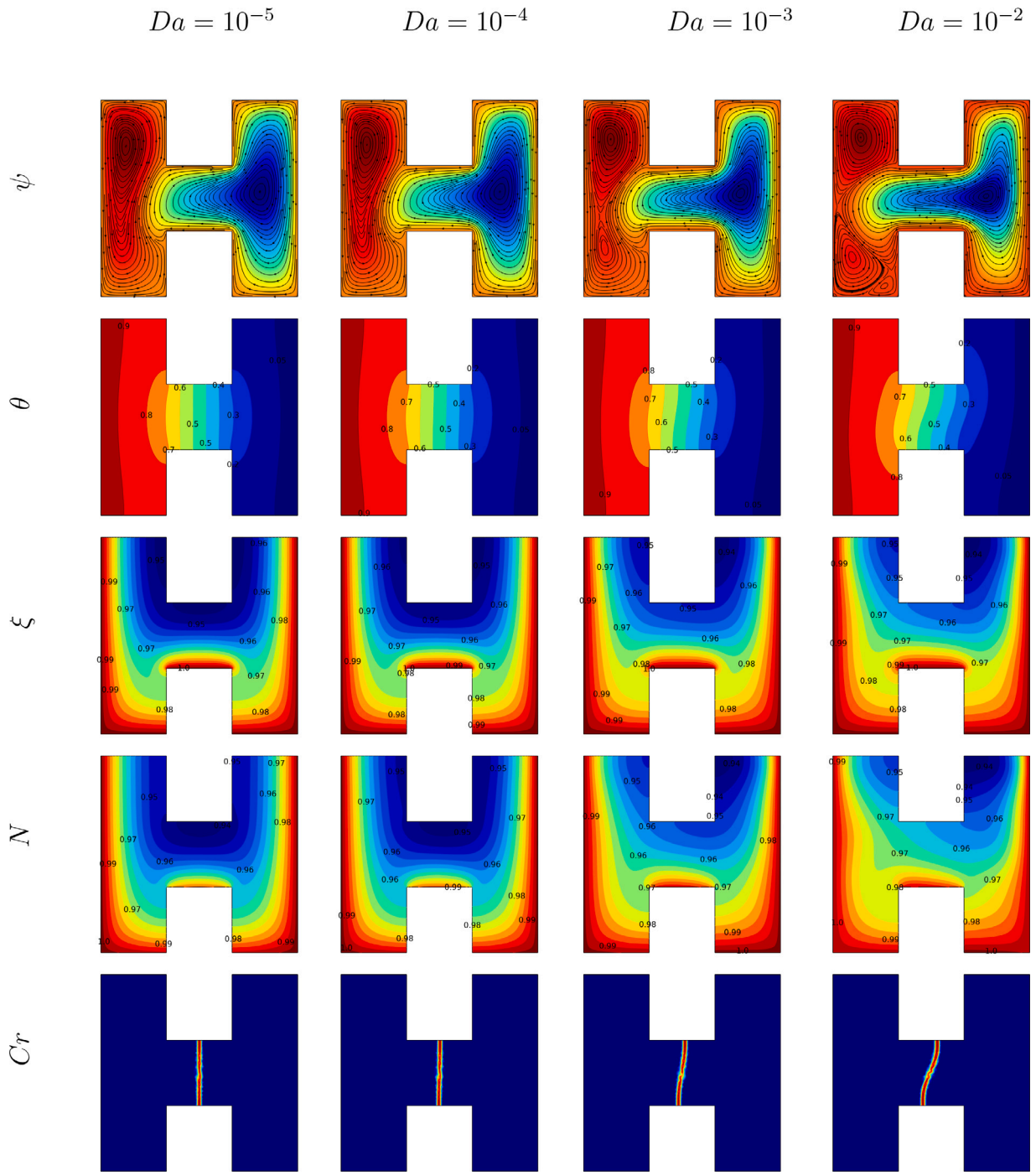

Fig. 5. The contours of ψ, θ, ξ, N, and Cr below the variations of Da at $Ste = \theta_f = 0.5, Ra = 10^5, Pr = 6.2, \chi = \zeta = 1, \gamma = 0, AR = 1/3, \epsilon = 0.8, \phi = 0.05, Ha = 25, Rd = 1, Le = Pe = 1$, and $R_b = 10$.

3. The Nusselt (Nu) and Sherwood (Sh) numbers

The corresponding quantities related to the rates of heat and mass transport are:

$$Nu_{\text{avg}} = -\frac{k_{m,b}}{k_f}\int_0^1 \frac{\partial \theta}{\partial X}dY, \quad Sh_{\text{avg}} = -\int_0^1 \frac{\partial \xi}{\partial X}dY. \tag{13}$$

4. Numerical procedure

The dimensionless form of a physical problem is solved by Galerkin finite element method. After achieving the weak formulation for system of Eqs. (6), a hybrid grid has been constructed discretized. All the solution components except the pressure have been discretized using the quadratic ($\mathbb{P}_2$) elements while the pressure is approximated by utilizing the ($\mathbb{P}_1$) finite elements. Adaptive Newtons method has been implemented to linearize the resulting system of nonlinear equations. Within each nonlinear sweep, the linear system of equations was resolved through the application of the Gaussian elimination method. The nonlinear outer loop terminated when the nonlinear residual decreased to 10^{-6}, with the last iteration deemed acceptable as the approximate solution. This technique has already been employed and explained in our earlier work, see [35,36] for details.

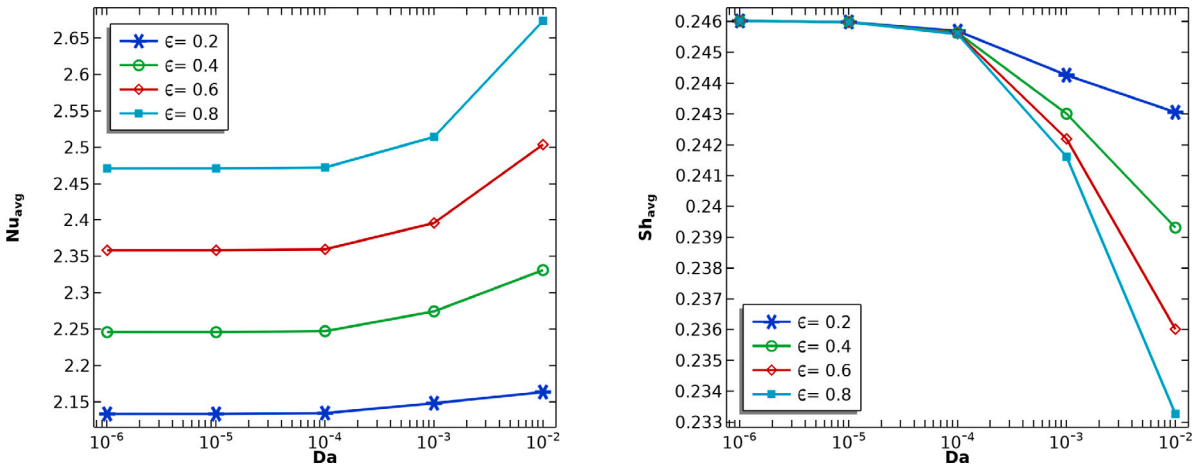

Fig. 6. The Nu_{avg} and Sh_{avg} under variations of ϵ and Da at $\chi = \zeta = 1, Ste = \theta_f = 0.5, \phi = 0.05, Ha = 25, Pr = 6.2, Le = Pe = 1, AR = 1/3, Ra = 10^5, \gamma = 0, Rd = 1,$ and $R_b = 10$.

Table 2
Comparison of the present study and available data of Ref. [38] for $\phi = 0.04$.

Ha	Nu_{avg}		$\lvert\psi\rvert_{\max}$	
	Present	Ref. [38]	Present	Ref. [38]
0	4.899	4.896	11.589	11.561
15	4.217	2.211	8.759	8.734
30	3.131	3.124	5.668	5.642
45	2.324	2.317	3.652	3.629
60	1.821	1.815	2.433	2.415

Table 3
The grid sensitivity analysis.

ℓ	Nu_{avg}	Sh_{avg}
1	2.558040	0.241041
2	2.542574	0.241400
3	2.540252	0.241448
4	2.522573	0.241624
5	2.521363	0.241662
6	2.522014	0.241662
7	2.516018	0.241664
8	2.514013	0.241607

4.1. The validation and grid sensitivity tests

The adopted solution has been validated in [37] against numerical and experimental studies. Further, in order to test the reliability of the designed solver for the MHD natural convection flow of nanofluid in a cavity, the present solver is validated for the against the available data of [38]. A close agreement of the results shown in Table 2 provided us the confident to carry out the simulations of the proposed problem.

The grid independence check is performed for the average Nu and Sh numbers for $Pr = 6.2, Da = 10^{-3}, Le = Pe = 1, \epsilon = 0.8, Ste = \theta_f = 0.5, \chi = \zeta = 1, \phi = 0.05, AR = 1/3, Ra = 10^5, Rd = 1, Ha = 25, \gamma = 0,$ and $R_b = 10$. The results are demonstrated in Table 3 which shows insignificant variations in the chosen quantities for the highest computed level $\ell = 8$. So, $\ell = 8$ is found appropriate for the numerical simulation.

5. ANN model development

Six different artificial neural networks (ANNs) have been established to forecast Nu_{avg} and Sh_{avg} values with an artificial intelligence approach. Six different ANN models were proposed because the independent input variables for the Nu_{avg} and Sh_{avg} values estimated at each stage were different. Multilayer perceptron (MLP) structure is used as the architecture in ANNs. MLP networks consist of layers and each layer is directly connected to each other. The first layer of the MLP network is the input layer, and in the input layer, input parameters are defined to the system. After the input layer, there is a hidden layer, and there is at least one hidden layer in each MLP network. The next layer after the hidden layer is the output layer where the prediction values are obtained. Independent variables were definite as input parameters in the input layer of the MLP network, and Nu_{avg} and Sh_{avg} values were gained in the output layer. There are 10 neurons in the hidden layer of each model. The basic architecture of the developed MLP network is shown in Fig. 2. Ideal grouping of the data set used in ANN models is one of the significant parameters that affects the prediction correctness of the model [39]. The methodology obtained from the literature was used to group the data set used in training the models [40]. 70% of the data was used for training the model, 15% for validation and 15% for testing. In each ANN model, Levenberg–Marquardt training algorithm was used as the training algorithm and Tan-Sig and Purelin functions were used as transfer functions. Performance parameters commonly used in the literature were discussed in order to investigate the training, learning and prediction accuracies of ANN models. The equations used to calculate the mean squared error (MSE), coefficient of determination (R) and margin of deviation (MoD) parameters, which were used as performance parameters, are given below [41]:

The performance parameters MSE, R and MoD can be written as [42]:

$$\text{MSE} = \frac{1}{N}\sum_{i=1}^{N}(X_{\text{targ}(i)} - X_{\text{ANN}(i)})^2 \tag{14}$$

$$\text{R} = \sqrt{1 - \frac{\sum_{i=1}^{N}(X_{\text{targ}(i)} - X_{\text{ANN}(i)})^2}{\sum_{i=1}^{N} X_{\text{trag}(i)}}} \tag{15}$$

$$\text{MoD} = \frac{\left[X_{\text{targ}} - X_{\text{ANN}}\right]}{X_{\text{targ}}} \times 100(\%) \tag{16}$$

6. CFD numerical results

This section introduces the representative visualizations of the performed numerical simulations under the pertinent physical parameters. The streamlines ψ, temperature θ, Oxygen ξ, Microorganisms, N, and heat capacity ratio Cr as well as Nu_{avg} and Sh_{avg} for different Hartmann number (Ha), inclination angle of a magnetic field γ, Darcy number (Da), cavity aspect ratio (AR), nanoparticles parameter (ϕ), Lewis number (Le), Péclet number (Pe), bioconvection Rayleigh (R_b), porosity parameter (ϵ), Rayleigh number (Ra), and radiation parameter (Rd) are conducted in Figs. 3, 4, 5, 6, 7, 8, 9, 10, 11, 12, and 13. The

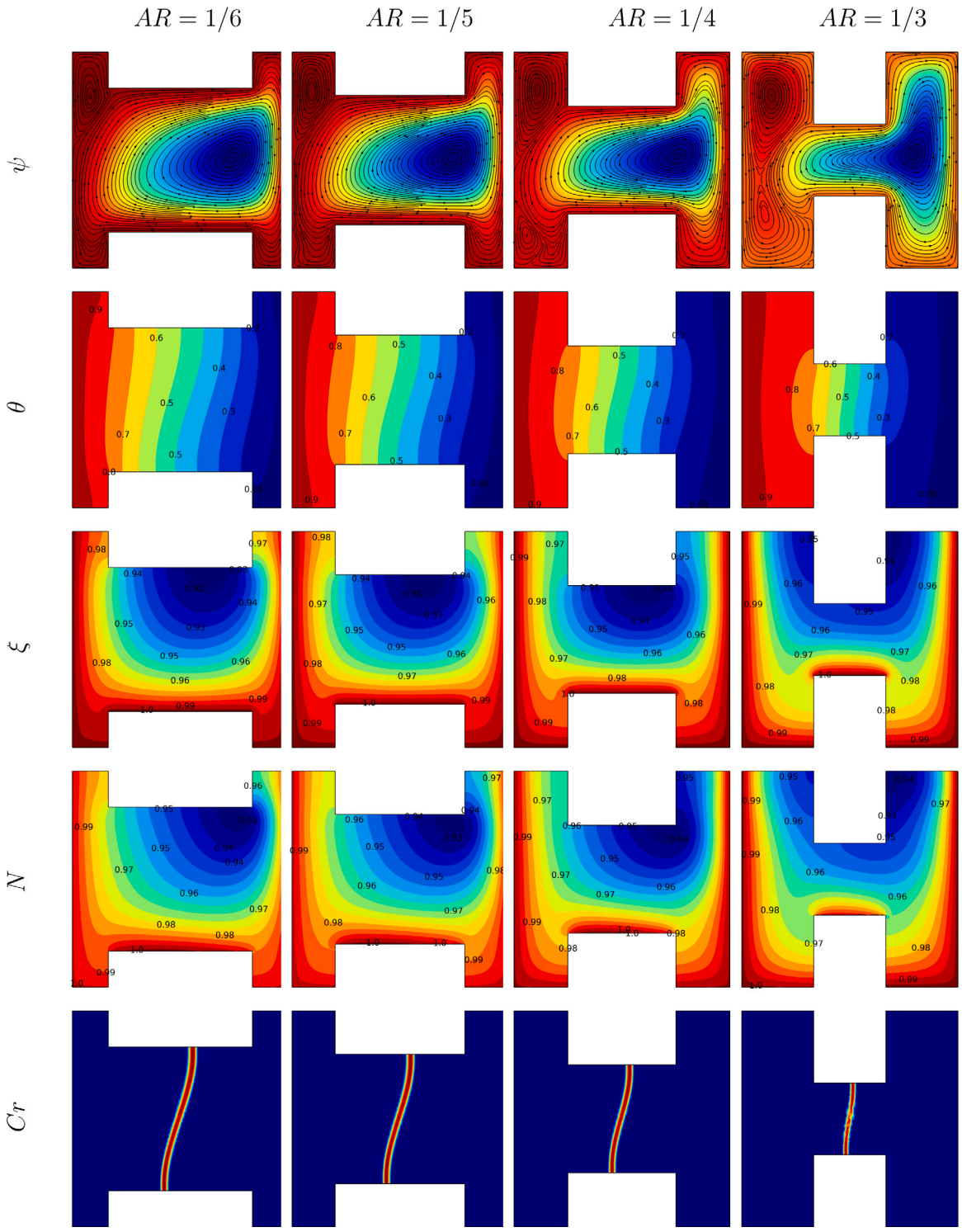

Fig. 7. The contours of ψ, θ, ξ, N, and Cr below the variations of AR at $Da = 10^{-3}$, $Le = Pe = 1$, $Ste = \theta_f = 0.5$, $\epsilon = 0.8$, $\chi = \zeta = 1$, $Pr = 6.2$, $\phi = 0.05$, $Ha = 25$, $\gamma = 0$, $Ra = 10^5$, $Rd = 1$, and $R_b = 10$.

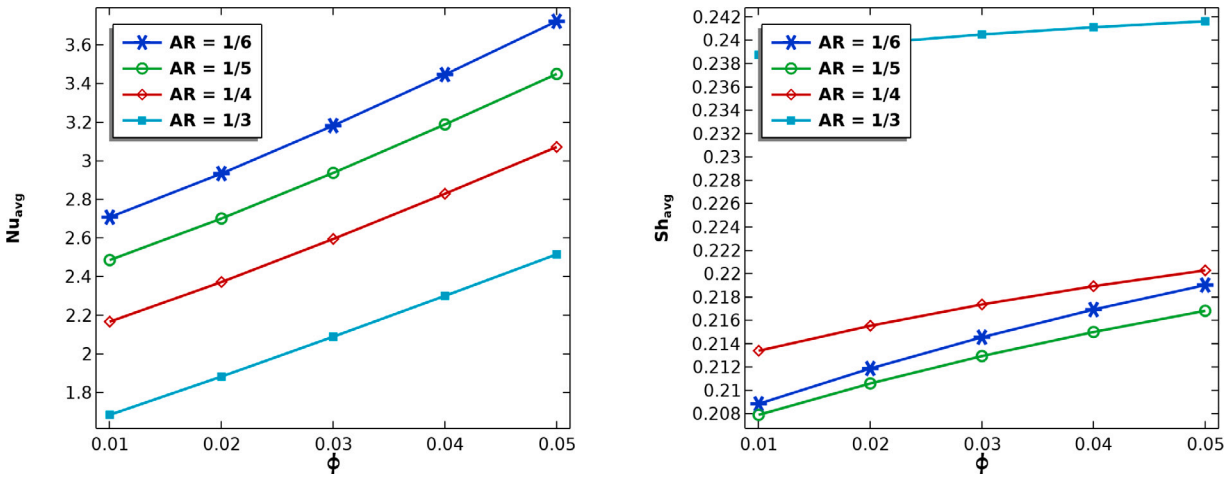

Fig. 8. The Nu_{avg} and Sh_{avg} below the impacts of AR with ϕ for $Ra = 10^5, Ste = \theta_f = 0.5, \chi = \zeta = 1, Pr = 6.2, Ha = 25, Da = 10^{-3}, \gamma = 0, Rd = 1, Le = Pe = 1, \epsilon = 0.8,$ and $R_b = 10$.

ranges of pertinent parameters are Hartmann number ($10 \le Ha \le 100$), an inclination angle ($15 \le \gamma \le 90$), Darcy number ($10^{-5} \le Da \le 10^{-2}$), cavity aspect ratio ($1/6 \le AR \le 1/3$, nanoparticles parameter ($0.01 \le \phi \le 0.05$), Rayleigh number $10^3 \le Ra \le 10^6$), porosity parameter ($0.2 \le \epsilon \le 0.8$), Péclet number ($0.1 \le Pe \le 1$), bioconvection Rayleigh ($0 \le R_b \le 20$), Lewis number ($1 \le Le \le 10$), and radiation parameter ($0 \le Rd \le 4$).

6.1. Effect of the Hartmann number (Ha)

Fig. 3 depicts the influences of Ha on the contours of ψ, θ, ξ, N, and Cr. Ha signifies the ratio of magnetic to viscous forces in a conductive fluid under a magnetic field. Physically, Ha gauges the relative influence of magnetic and viscous effects in fluid flow. A high Ha indicates magnetic dominance, altering flow behavior significantly. Conversely, a low Ha suggests viscous forces prevail. Physically, Lorentz force powers by an increment in Ha and this force shrinks the nanofluid velocity. As a result, an increment in Ha declines the strength of ψ across H-shaped cavity. The uniform streamlines are appearing at low $Ha = 10$, while according to an extra of Ha, the streamlines contour is shrinking on the right area of H-shaped cavity. Further, the isotherms are affected by variation of Ha. The contours of oxygen and microorganisms are reducing across H-shaped cavity as Ha increases. The region of a phase change is slightly shifted by an increment in Ha due to the less contributions of Ha in changing heat transfer within H-shaped cavity.

Fig. 4 presents Nu_{avg} and Sh_{avg} under the variations of Ha and γ. Here, the values of Nu_{avg} are decreasing according to an increment in Ha. The alterations of Nu_{avg} are appearing clearly at lower Ha and Nu_{avg} declines as γ boosts from 15° to 90°. The values of Sh_{avg} are enhanced according to an increment in Ha and γ. At $\gamma = 90°$, the values of Nu_{avg} declines by 1.67% and Sh_{avg} increases by 0.247 as Ha increases from 10 to 100.

6.2. Effect of the Darcy number (Da)

Fig. 5 indicates the influences of Da on the contours of ψ, θ, ξ, N, and Cr. Physically, Da plays the factor of a porous resistance of the nanofluid flows. Da reveals the influence of pressure gradients and viscous forces on fluid flow through porous materials. A high Da suggests pressure gradients drive flow, while a low one indicates significant viscous resistance within the porous medium. Knowledge of the Da is critical in engineering and geophysical fields, such as groundwater flow, oil reservoir modeling, and soil permeability analysis. It aids in predicting fluid behavior and optimizing processes involving porous media flow. Consequently, increasing Da reduces the porous resistance and enhances the nanofluid velocity. The strength of ψ is enhanced as Da increases du to a low porous resistance. The isotherms are enhanced across the right area of H-shaped cavity when Da increases. Also, the contours of ξ, and N are clearly improved as Da increases. The phase change zone in the cavity's center shifts towards the left area according to an increment in Da.

The impacts of Da, and ϵ on the values of Nu_{avg} and Sh_{avg} are introduced in Fig. 6. Since the porous permeability increases by a decrease in ϵ, then the value of Nu_{avg} decreases by a reduction in ϵ. While, the value of Sh_{avg} enhances by a reduction in ϵ. Further, a decrease in Da enhances Nu_{avg} and reduces Sh_{avg}. Physically, the changes of intensity of bioconvection flow according to the changes of the porous resistance.

6.3. Effect of the cavity aspect ratio (AR)

Fig. 7 shows the effects of AR on the contours of ψ, θ, ξ, N, and Cr. The cavity aspect ratio AR offers understanding of a cavity's shape and size and how they impact flow or heat transfer. A high aspect ratio signifies elongation, while a low one indicates a squat shape. This insight aids in optimizing systems involving cavities, like in electronics cooling, combustion chambers, and aerodynamics. Because of changes in H-shaped geometry due to the alterations on AR, the contours of ψ are altered by the variations of AR. The uniform distributions of streamlines are established clearly when AR increases from 1/6 to 1/3. Hence, the geometry's factor plays a well role in adjusting the bioconvection flow within a closed domain. Also, the isotherms are extended according to the lower values of AR. There are changes on the contours of ξ, and N, according to the variations of AR. The phase change zone is shrinking across the cavity's center as AR increases from 1/6 to 1/3.

Fig. 8 presents the Nu_{avg} and Sh_{avg} for different values of AR with ϕ. Increasing AR declines the values of Nu_{avg} and enhances Sh_{avg}. Adding extra concentration of nanoparticles from 1% to 5% enhances the values of Nu_{avg} and Sh_{avg}.

6.4. Effect of the Rayleigh number (Ra)

Fig. 9 introduces the impacts of Ra on the contours of ψ, θ, ξ, N, and Cr. Physically, Ra accelerates the bioconvection flow by boosting the buoyancy forces. Ra is a dimensionless quantity used in fluid dynamics and heat transfer to characterize the relative significance of buoyancy forces to viscous forces within a fluid undergoing convective motion due to thermal gradients. A high Ra signals buoyancy forces overpowering viscosity, triggering convection due to temperature gradients. Conversely, a low Rayleigh number implies viscosity dominates, resulting in mainly laminar flow without notable convection. Accordingly,

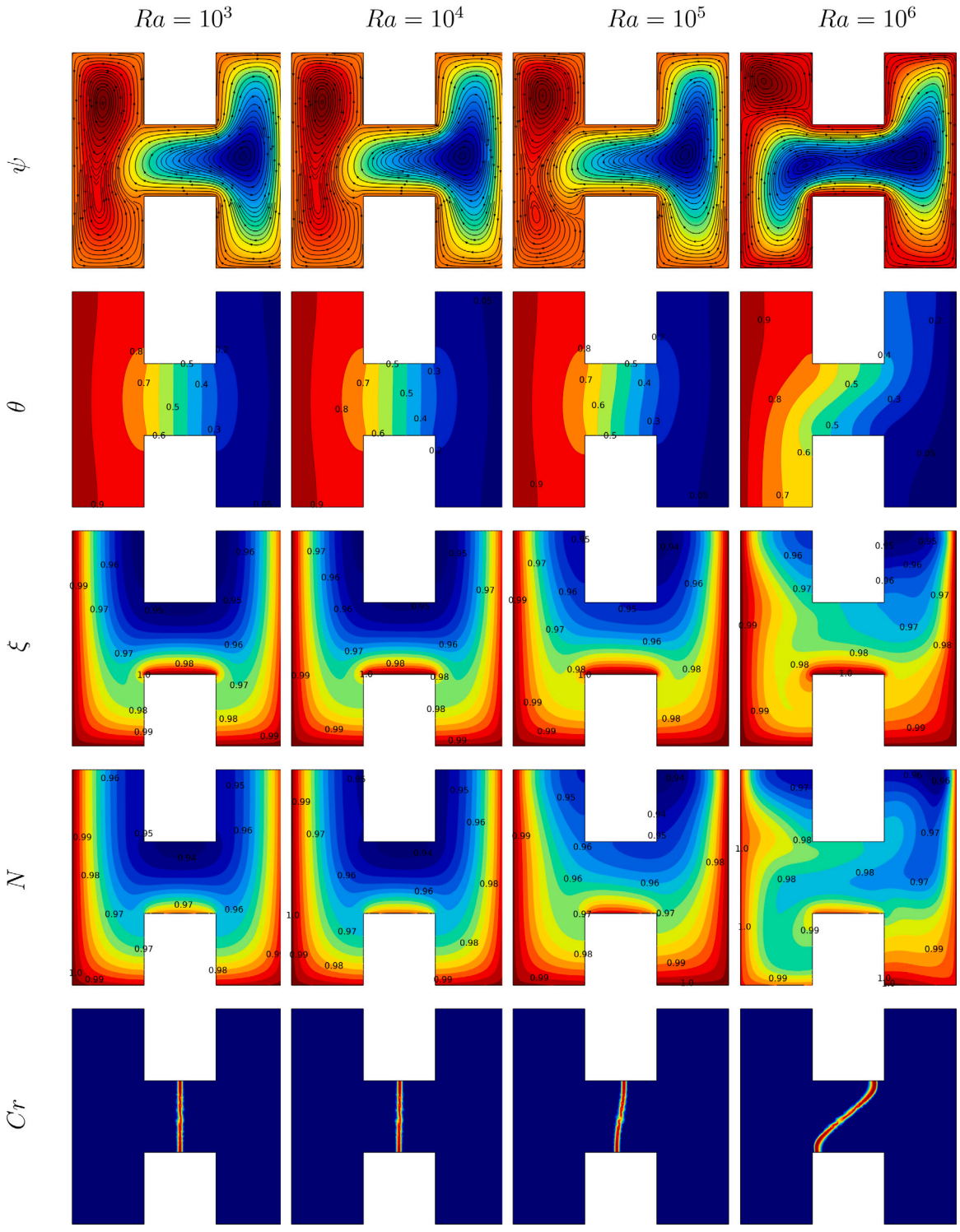

Fig. 9. The contours of ψ, θ, ξ, N, and Cr below the variations of Ra at $Ste = \theta_f = 0.5, Da = 10^{-3}, Ha = 25, \phi = 0.05, \chi = \zeta = 1, Pr = 6.2, \epsilon = 0.8, Le = Pe = 1, \gamma = 0, AR = 1/3, Rd = 1$, and $R_b = 10$.

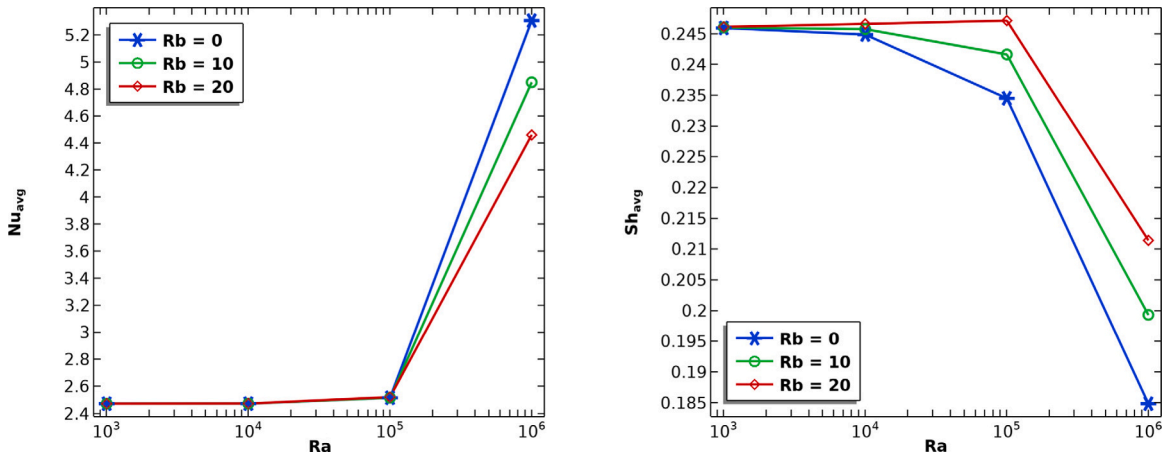

Fig. 10. The Nu_{avg} and Sh_{avg} under the impacts of R_b and Ra at $Da = 10^{-3}, Ste = \theta_f = 0.5, Pr = 6.2, Le = Pe = 1, Ha = 25, \gamma = 0, \epsilon = 0.8, AR = 1/3, \phi = 0.05, Rd = 1,$ and $\chi = \zeta = 1$.

the strength of ψ increases by an increment in Ra. Also, the contours of θ, ξ, and N are improved according to an increase in Ra. The phase change zone shifts towards the right area according to an increase in Ra. These results are representing the importance of Ra in improving the bioconvection flows.

Fig. 10 shows the influences of R_b and Ra on the values of Nu_{avg} and Sh_{avg}. Here, an increase in Rb reduces Nu_{avg} and improves Sh_{avg}. Further, an increase in Ra enhances Nu_{avg} and reduces Sh_{avg}.

6.5. Effect of the Lewis number (Le)

Fig. 11 presents the contours of ψ, θ, ξ, N, and Cr under the variations of Le. Physically, Le represents the ratio amongst thermal to mass diffusivity. A high Le means heat diffuses faster than mass, indicating thermal diffusion dominance, while a low Le suggests mass diffusivity prevails over thermal diffusivity. Comprehending Le is vital in fields like combustion, chemical reactions, and transport phenomena, aiding in predicting heat and mass transfer rates in fluids. Consequently, increasing Le suppresses the intensity of the streamlines across H-shaped cavity. The contours of oxygen and microorganisms are enhanced relevant to an augmentation in Le. The changes on Le has minor influences in Cr.

The values of Nu_{avg} and Sh_{avg} for different values of Pe and Le are introduced in Fig. 12. An augmentation in Pe reduces the value of Nu_{avg} and enhances Sh_{avg}. Fig. 13 shows the values of Nu_{avg} and Sh_{avg} under the changes on radiation parameter Rd and ϕ. Physically, Rd relates transfer of a conduction to thermal radiation. As a result, the values of Nu_{avg} are enhanced according to an augmentation in Rd and ϕ. Sh_{avg} increases as ϕ boosts and their values are reduced when Rd increases.

7. ANN model results

To investigate the prophecy performance for the ANN models, firstly, the prediction values gained from the ANN models were associated with the target values. In Figs. 14 and 15, Nu_{avg} and Sh_{avg} are computed from the ANN archetypal and target values are given for separately data point. For each data point, it can be perceived that the values gotten from the ANN model and the data expressing the target values are in ideal harmony. This ideal harmony of the Nu_{avg} and Sh_{avg} values contracted from the ANN model with the target values indications that the established ANN models can foresee the Nu_{avg} and Sh_{avg} values with extraordinary accurateness. Figs. 16 and 17 show the deviation rates between the Nu_{avg} and Sh_{avg} values gotten from the ANN archetypal and the target values. When the values given for each data point are surveyed, it is perceived that the points expressing the deviation rates are generally neighboring to the zero deviation line. Low deviation rates mean that the deviation in the middle of the Nu_{avg} and Sh_{avg} values attained from the ANN and the target values is low. The results gotten from the deviation rates show that the settled ANN models are adept of predicting Nu_{avg} and Sh_{avg} values with identical truncated fault rates. In order to accomplish a supplementary exhaustive fault scrutiny of ANN models, the alterations amongst the target values for each output parameter and the values achieved from the ANN model are shown in Figs. 18 and 19. When the difference values calculated for each data point are scanned, it is seen that generally very low error values are obtained. The small difference amongst the values gotten from the ANN model and the target values confirms that the technologically advanced ANN models are talented of predicting Nu_{avg} and Sh_{avg} values with very low errors. The target values are shown on the x-axis of Figs. 20 and 21, and the Nu_{avg} and Sh_{avg} values acquired from the ANN model are shown on the y-axes, respectively. When the locations of the data points are examined, it is realized that generally all data points are positioned on and near the zero error line. When the performance parameters given in Table 4 are scrutinized, it is grasped that the MSE values are identical stumpy, while the R values are premeditated very close to 1. All these results clearly prove that the 6 diverse ANN representations industrialized can foresee Nu_{avg} and Sh_{avg} values with very extraordinary accurateness.

8. Conclusions

This work computationally investigated the impacts of different Hartmann number, inclination angle of a magnetic field, bioconvection Rayleigh, Darcy number, porosity parameter, cavity aspect ratio, nanoparticles parameter, Péclet number, Rayleigh number, Lewis number, and radiation parameter on bioconvection flow of oxytactic microorganisms in H-type cavity. In this work, the streamlines, isotherms, heat capacity ratio, oxygen and microorganisms as well as Nu_{avg} and Sh_{avg} were calculated for the pertinent parameters.

The important numerical results of this work are listed as follow:

- Alternating H-type geometry by variations of cavity aspect ratio AR has a well role in controlling the bioconvection flow and phase change material.
- The Hartmann number shrinks the nanofluid velocity and deduces the contours of oxygen and microorganisms.
- Increasing Darcy parameter helps in deducing the porous resistance which enhances the intensity of isotherms, streamlines, oxygen and microorganisms.
- The bioconvection Rayleigh and Rayleigh numbers are effective in enhancing bioconvection flow and varying phase change material.

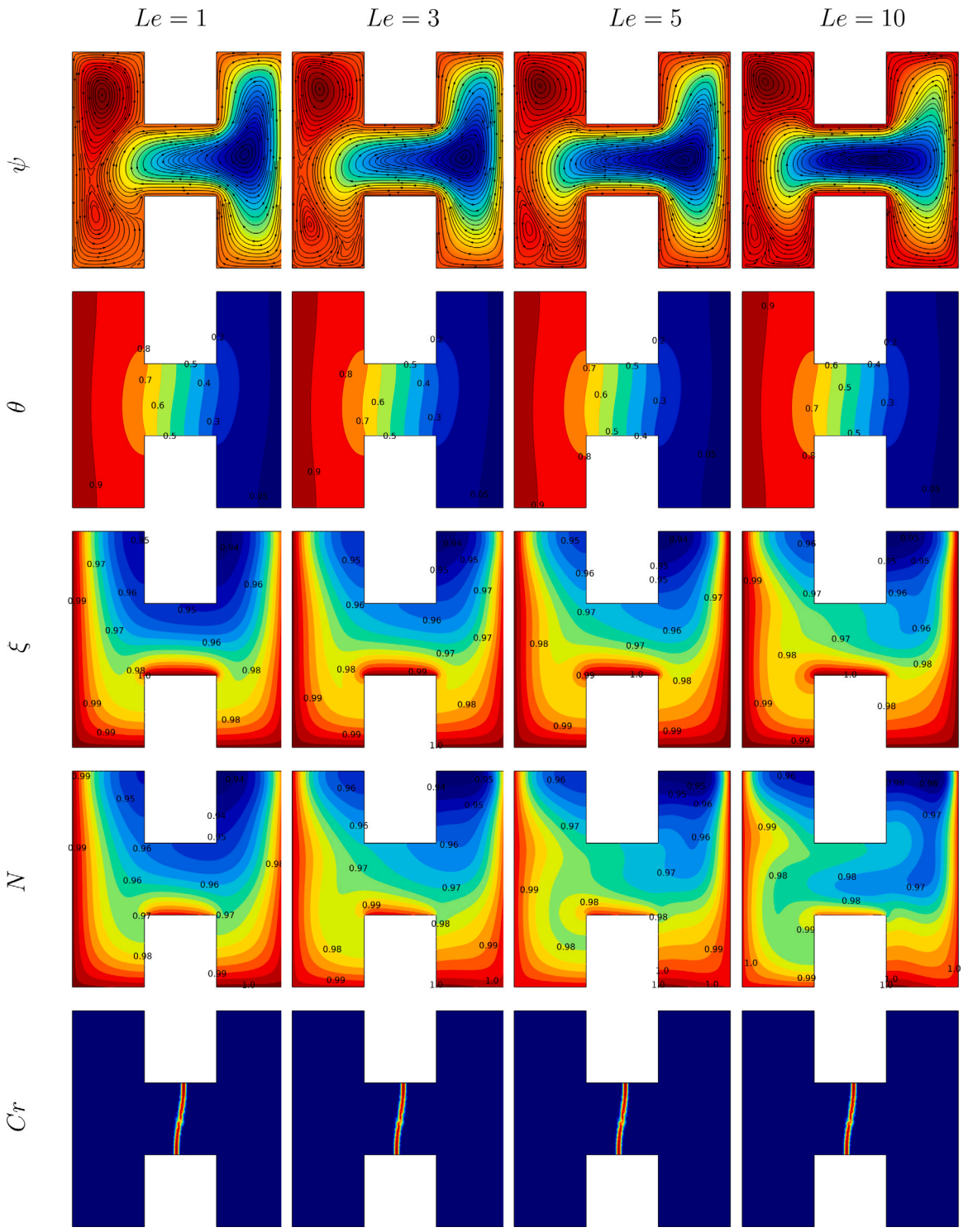

Fig. 11. The contours of ψ, θ, ξ, N, and Cr below the variations of Le for $Ste = \theta_f = 0.5, \phi = 0.05, Ha = 25, Da = 10^{-3}, Pr = 6.2, \epsilon = 0.8, Ra = 10^5, \gamma = 0, AR = 1/3, \chi = \zeta = 1, Rd = 1, Le = 1,$ and $R_b = 10$.

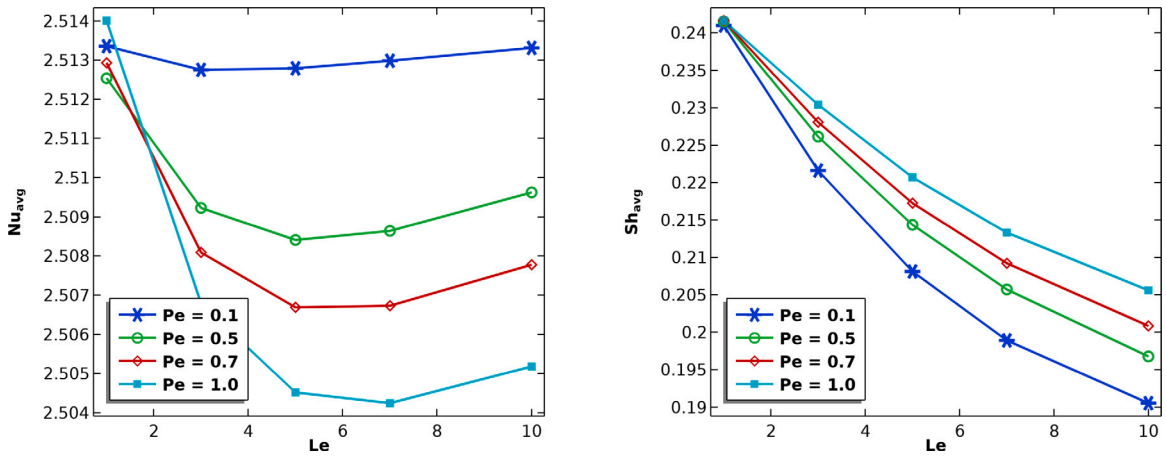

Fig. 12. The Nu_{avg} and Sh_{avg} under the impacts of Pe with Le for $Ra = 10^5, Ste = \theta_f = 0.5, \chi = \zeta = 1, \phi = 0.05, Pr = 6.2, Da = 10^{-3}, Ha = 25, \gamma = 0, AR = 1/3, Rd = 1, \epsilon = 0.8,$ and $R_b = 10$.

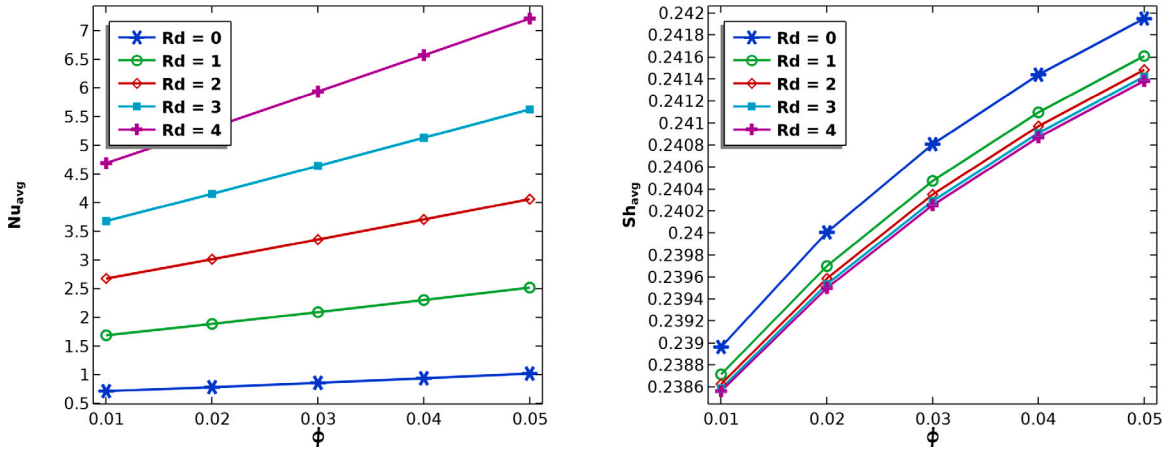

Fig. 13. The Nu_{avg} and Sh_{avg} under the impacts of Rd with ϕ for $Da = 10^{-3}, \chi = \zeta = 1, Ra = 10^5, Ste = \theta_f = 0.5, Pr = 6.2, Ha = 25, \epsilon = 0.8, AR = 1/3, Le = Pe = 1, \gamma = 0,$ and $R_b = 10$.

Table 4
Performance parameters for the ANN models.

	Model-1	Model-2	Model-3	Model-4	Model-5	Model-6
MSE	6.62E−10	1.04E−07	9.19E−06	8.97E−09	2.02E−05	3.23E−08
R	0.99999	0.99999	0.99997	0.99999	0.99995	0.99999

- The distributions of oxygen and microorganisms are improving across H-type cavity according to an increment in Lewis number.
- The values of Nu_{avg} are enhancing according to an increment in porosity parameter, Darcy parameter, bioconvection Rayleigh number, Rayleigh number, thermal radiation parameter, and nanoparticles parameter. While, the Nu_{avg} deduces as an augmentation in Hartmann number, cavity aspect ratio, a slope angle of a magnetic field, Péclet number, and Lewis number.
- Due to the difference of temperature amongst the left/right area of H-type cavity, the phase change zone appears in the center area between them.
- MSE values computed from ANN models were found to be smaller than 2.02E−05.
- R values for each model were calculated to be higher than 0.9999.
- With an increase in Ha from 10 to 100 at $\gamma = 90°$, the values of Nu_{avg} decreases by 1.67%, while Sh_{avg} increases by 0.247%.
- The obtained results demonstrated that the ANN models developed in this study can predict the high accuracy.

Future works

Future research will investigate the interaction between NEPCM and oxytactic microorganisms using advanced multi-phase modeling

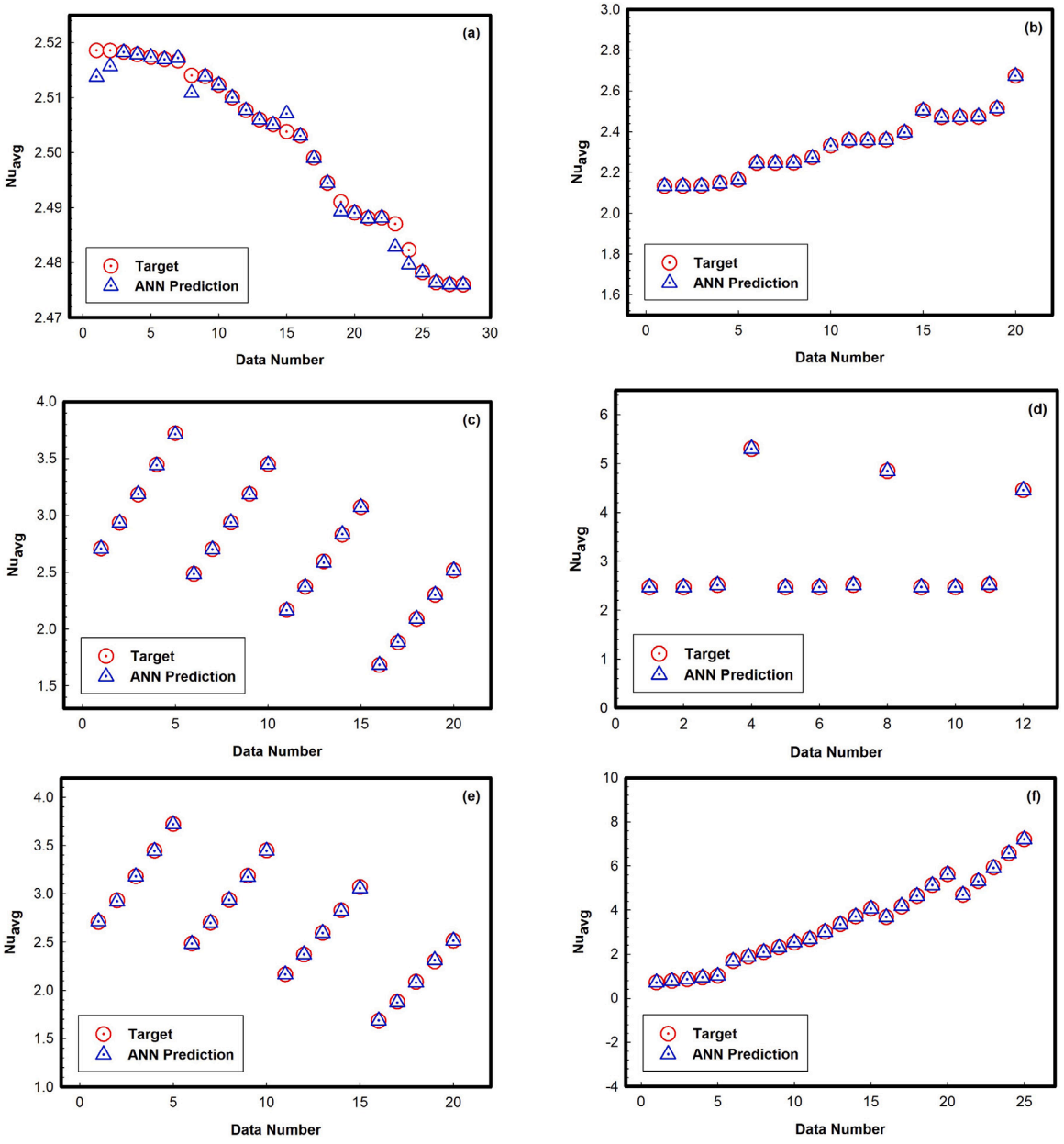

Fig. 14. Compatibility of Nu_{avg} values from the ANN-model and target-values.

to capture system behavior accurately. Additionally, the effects of nanoparticle types and concentrations on NEPCM's thermal and rheological properties will be explored, potentially through experimental validation for specific applications. Strategies to optimize system performance, including controlling microorganism distribution and manipulating magnetic fields for improved heat transfer efficiency, may be explored using optimization techniques like genetic algorithms or machine learning.

CRediT authorship contribution statement

Shafqat Hussain: Writing – original draft, Visualization, Validation, Software, Methodology, Investigation, Formal analysis, Conceptualization. **Abdelraheem M. Aly:** Writing – original draft, Visualization, Formal analysis, Conceptualization. **Noura Alsedias:** Writing – review & editing, Writing – original draft, Conceptualization. **Andaç Batur Çolak:** Writing – original draft, Software, Data curation.

Declaration of competing interest

The authors declare that they have no known competing financial interests or personal relationships that could have appeared to influence the work reported in this paper.

Data availability

Data will be made available on request.

Acknowledgments

Second author (Abdelraheem M. Aly) extend his appreciation to the Deanship of Scientific Research at King Khalid University, Abha, Saudi Arabia, for funding this work through the Research Group Project under Grant Number (RGP. 2/38/45). This research was funded by the Princess Nourah bint Abdulrahman University Researchers Supporting Project number (PNURSP2024R102), Princess Nourah bint Abdulrahman University, Riyadh, Saudi Arabia.

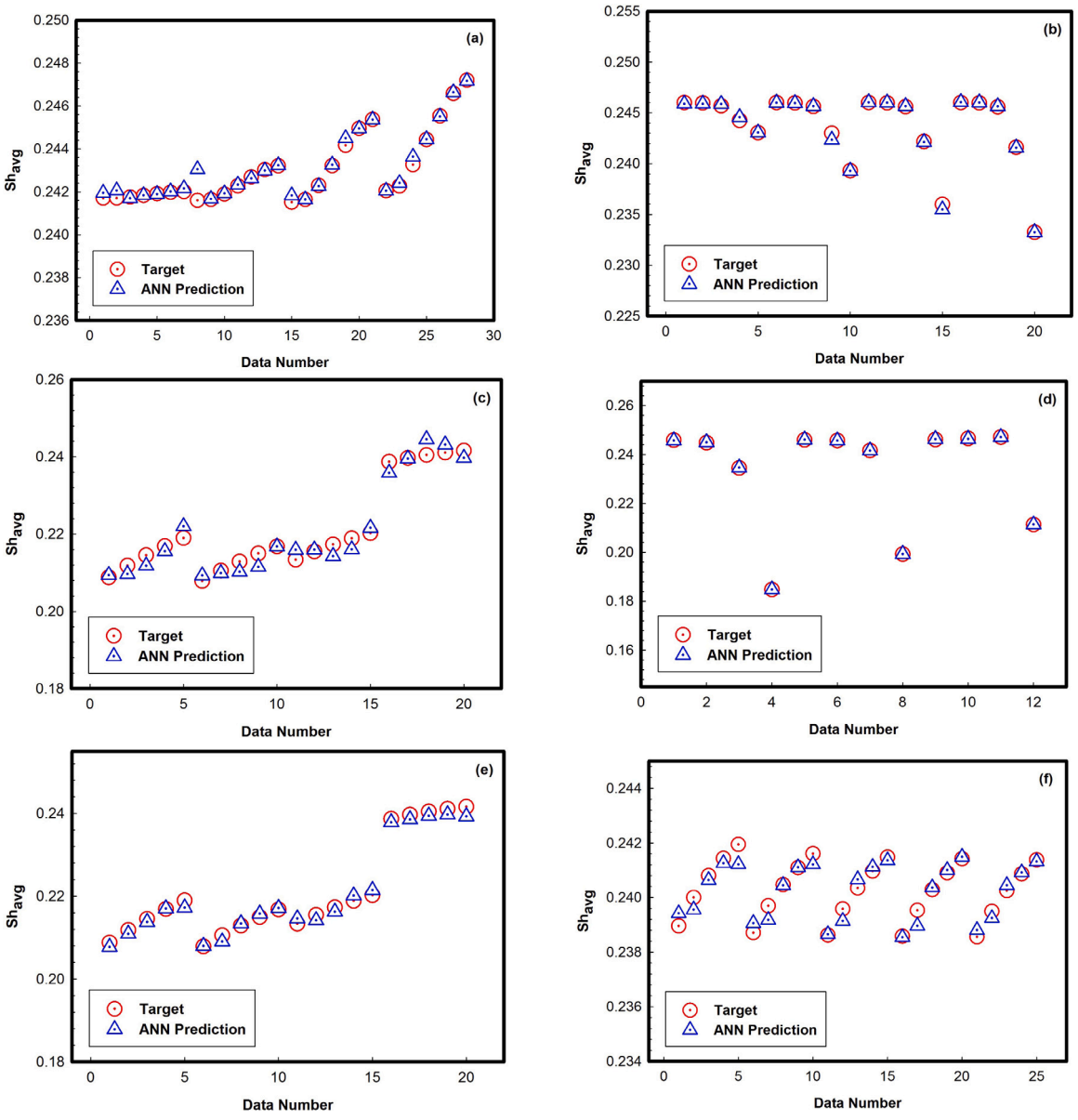

Fig. 15. Compatibility of Sh_{avg} values from the ANN-model and target-values.

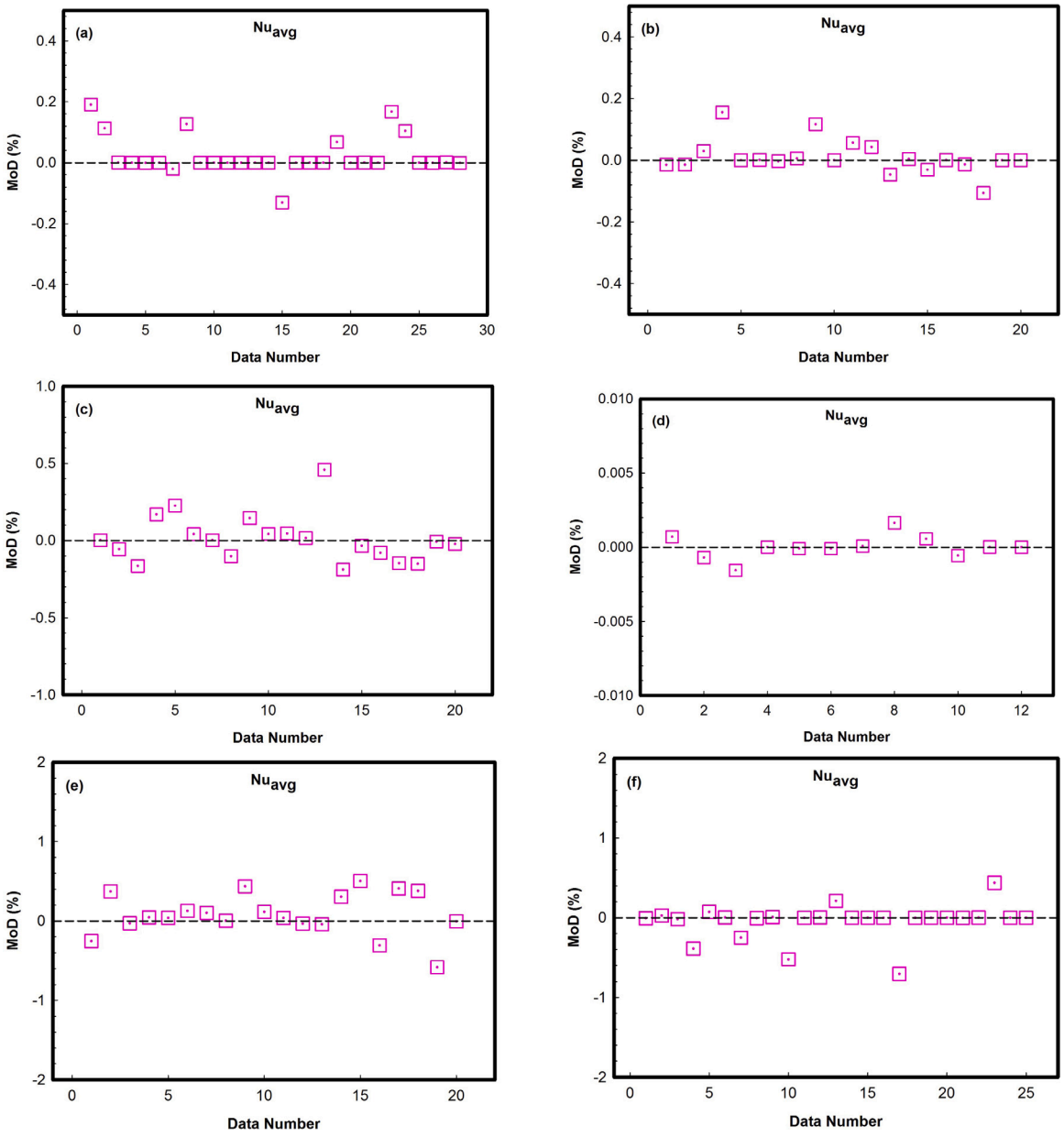

Fig. 16. Deviation rates between Nu_{avg} values from the ANN-model and target-values.

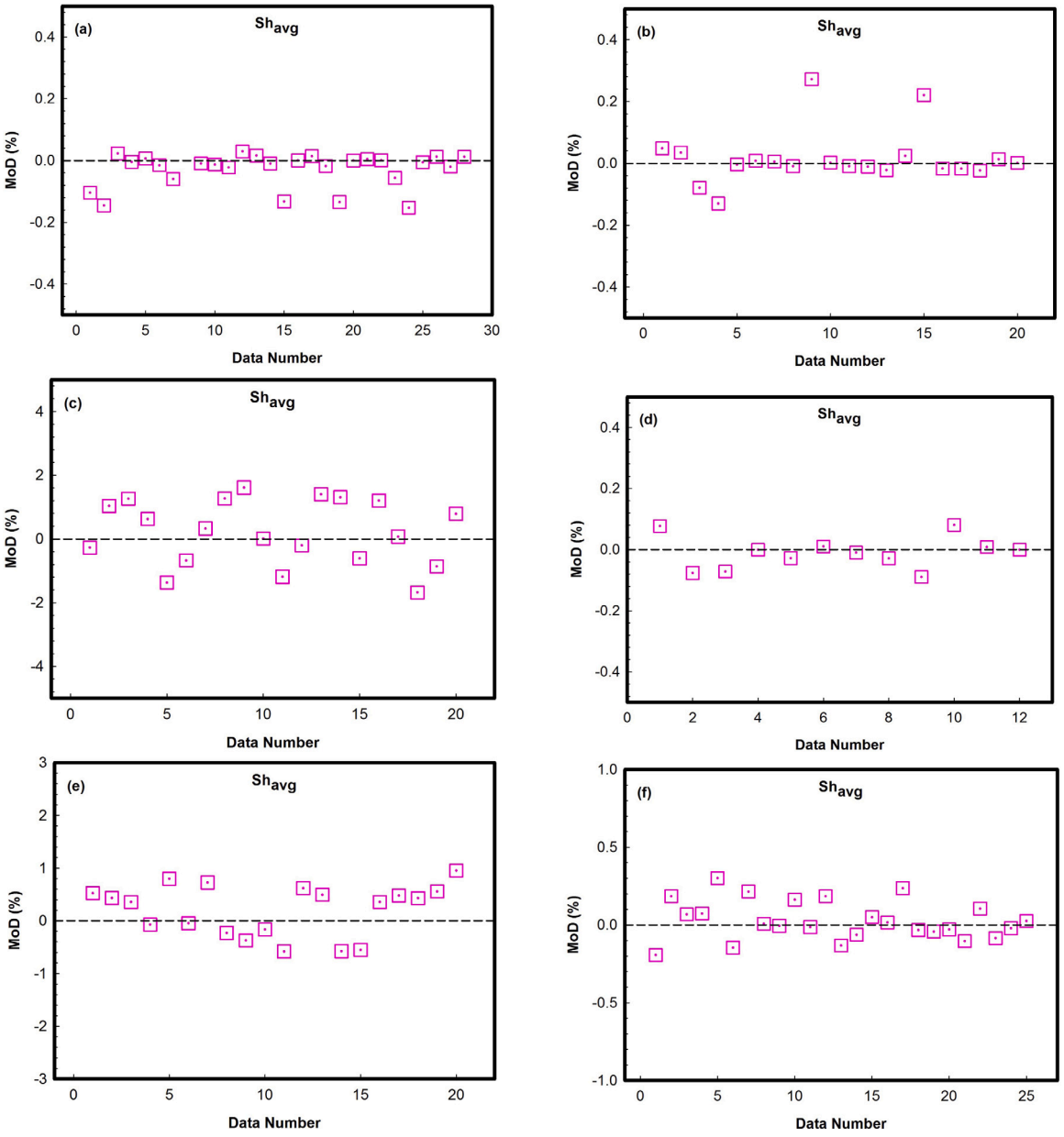

Fig. 17. Deviation rates between Sh_{avg} values from the ANN-model and target-values.

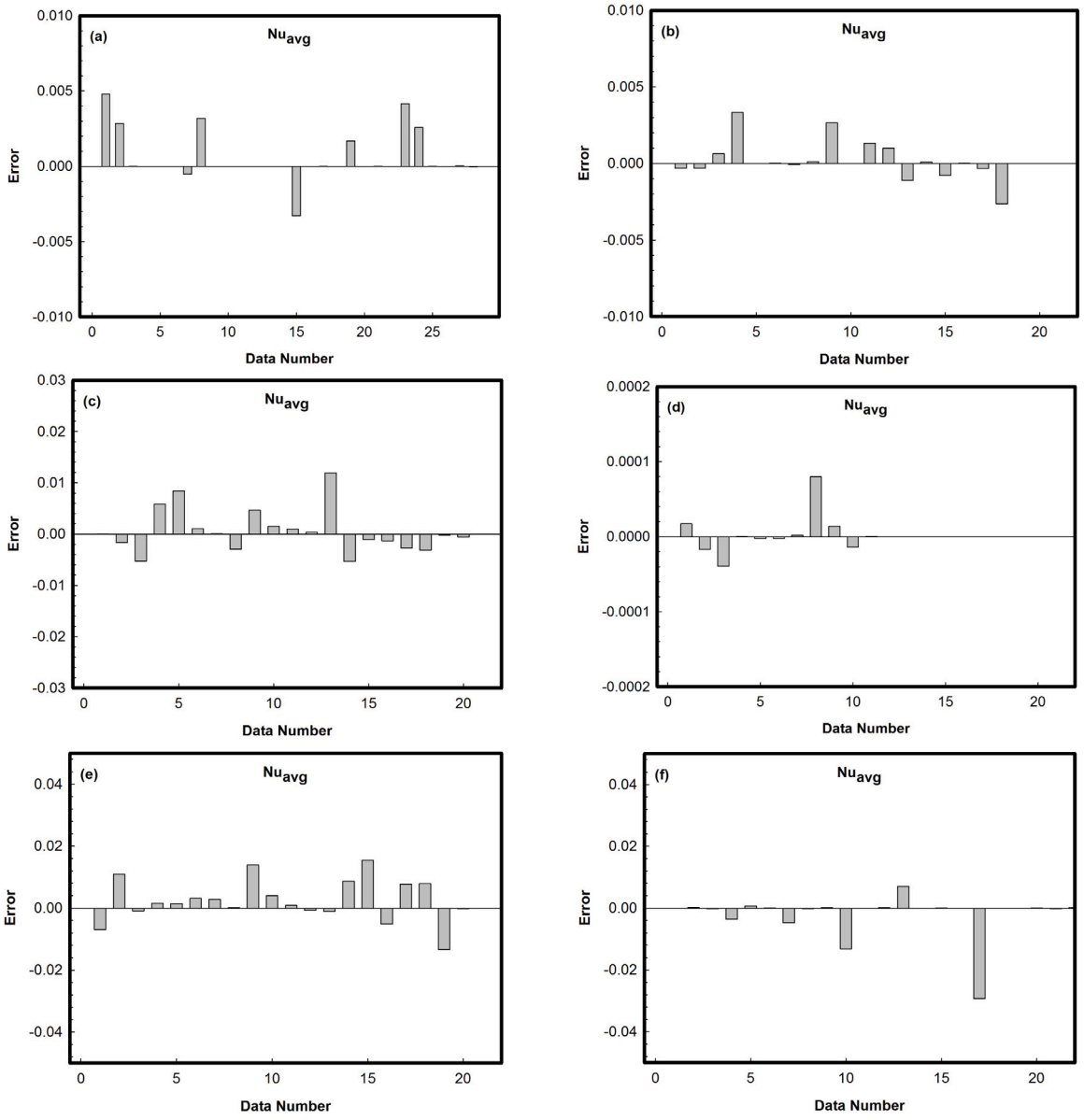

Fig. 18. Error values between Nu_{avg} values from the ANN-model and target-values.

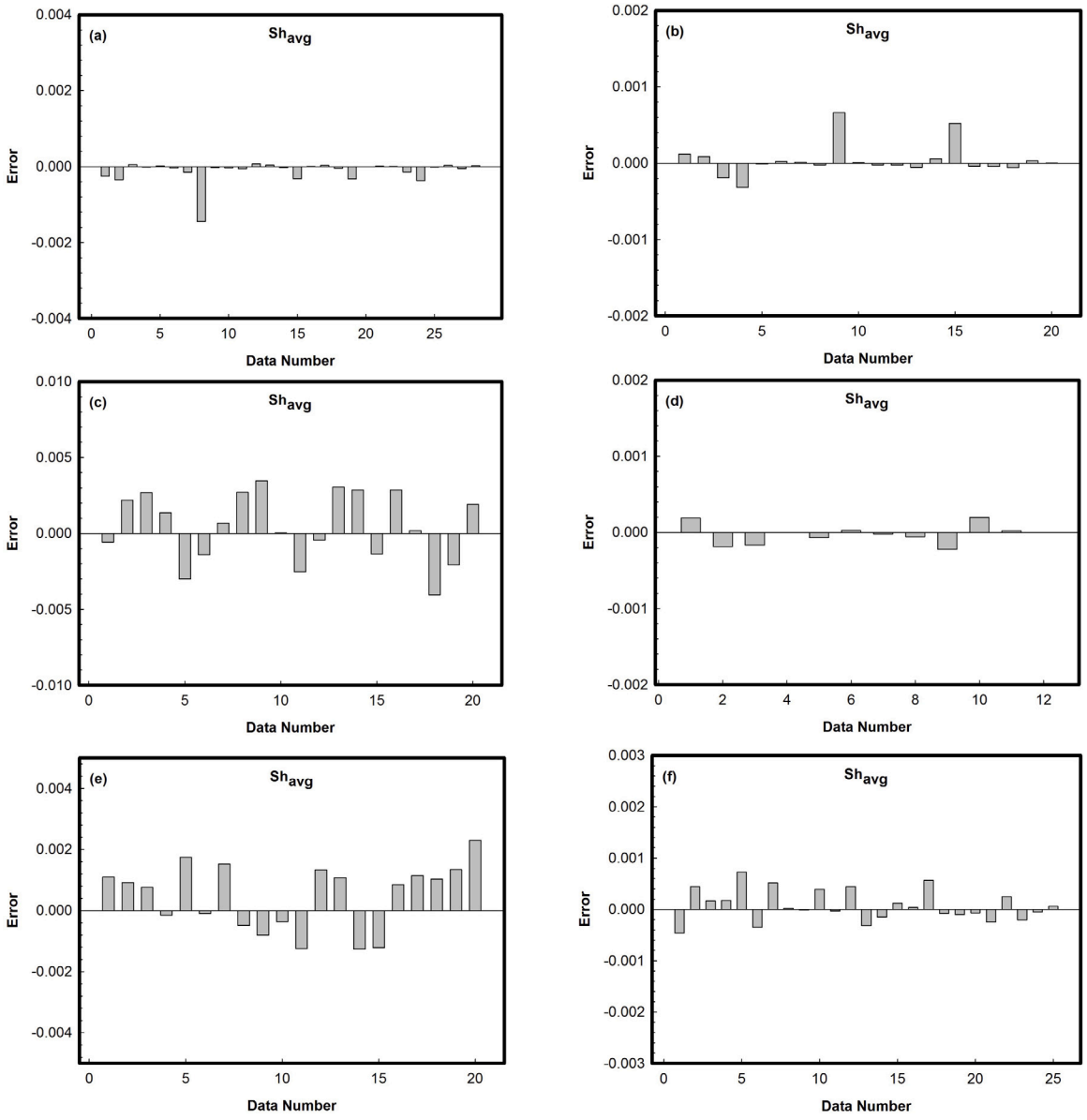

Fig. 19. Error values between Sh_{avg} values from the ANN-model and target-values.

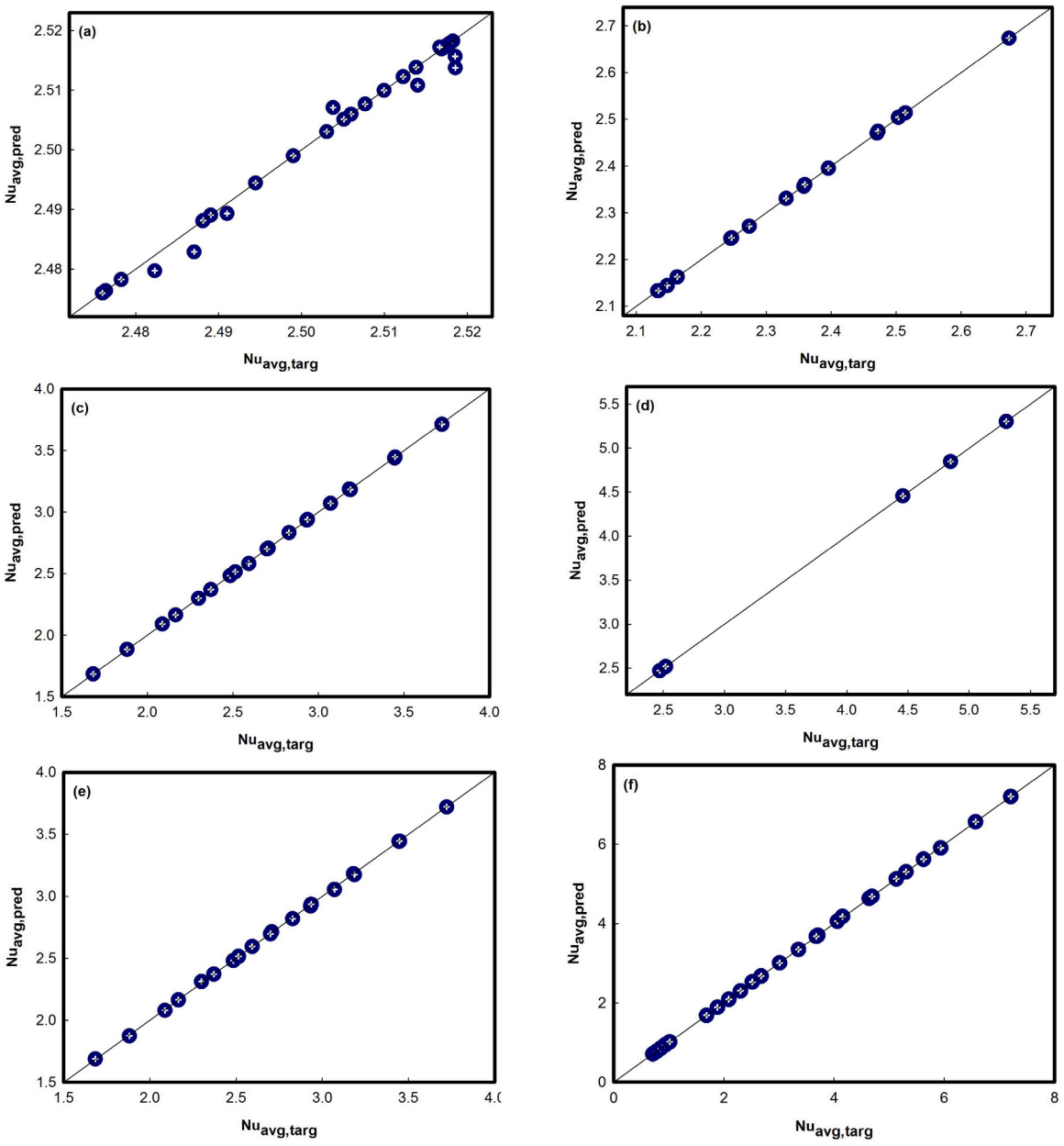

Fig. 20. The Nu_{avg} and target values from the ANN model.

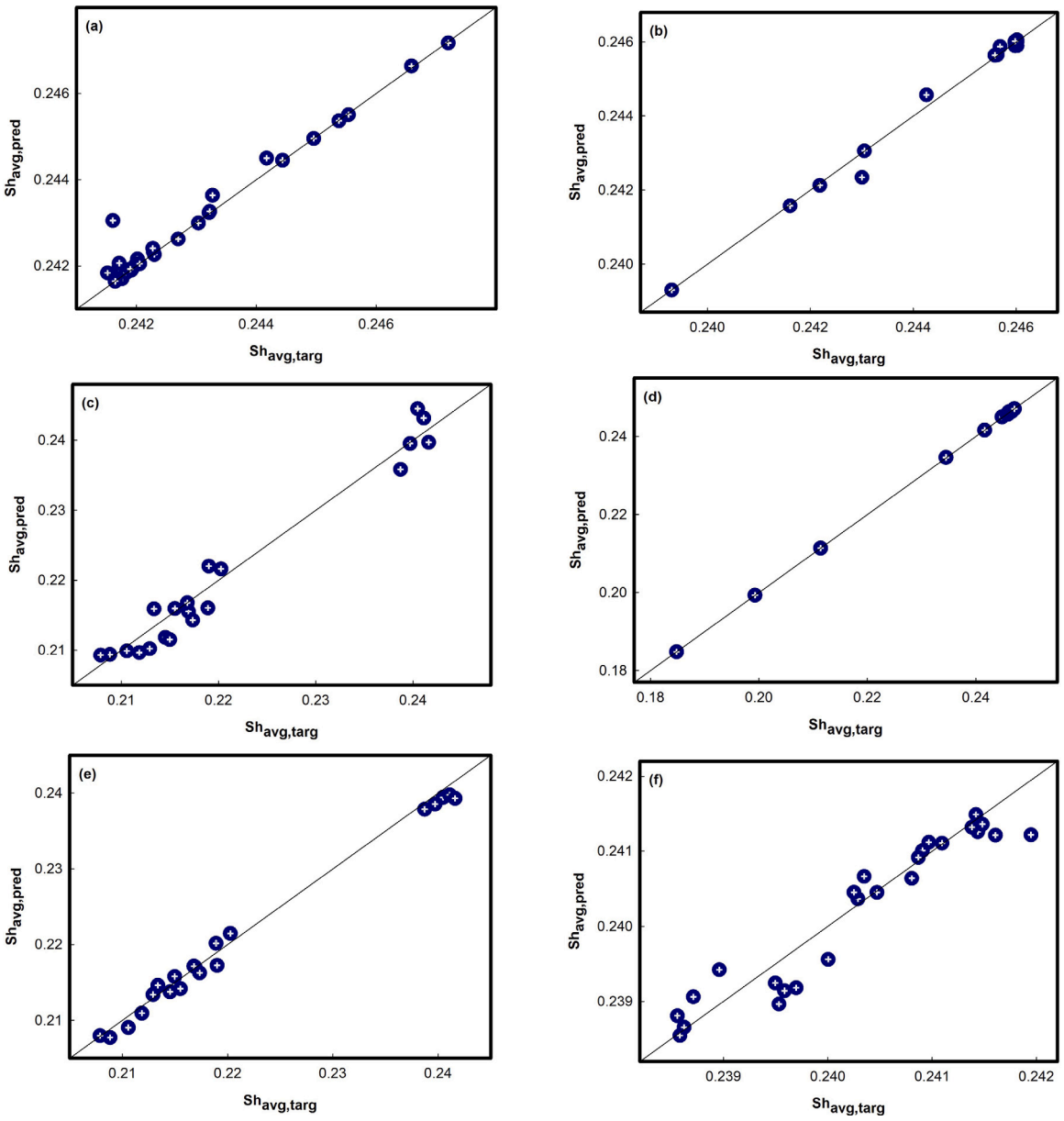

Fig. 21. The Sh_{avg} and target values from the ANN model.

References

[1] J.R. Platt, "Bioconvection Patterns" in cultures of free-swimming organisms, Science 133 (3466) (1961) 1766–1767.

[2] T. Sharma, A.L. Mohana Reddy, T. Chandra, S. Ramaprabhu, Development of carbon nanotubes and nanofluids based microbial fuel cell, Int. J. Hydrogen Energy 33 (22) (2008) 6749–6754.

[3] D.-S. Kim, H.S. Fogler, Biomass evolution in porous media and its effects on permeability under starvation conditions, Biotechnol. Bioeng. 69 (1) (2000) 47–56.

[4] T.L. Stewart, H.S. Fogler, Biomass plug development and propagation in porous media, Biotechnol. Bioeng. 72 (3) (2001) 353–363.

[5] B. Shen, L. Zheng, C. Zhang, X. Zhang, Bioconvection heat transfer of a nanofluid over a stretching sheet with velocity slip and temperature jump, Therm. Sci. 21 (6 Part A) (2017) 2347–2356.

[6] F.T. Zohra, M. Uddin, A. Ismail, O.A. Bég, A. Kadir, Anisotropic slip magneto-bioconvection flow from a rotating cone to a nanofluid with Stefan blowing effects, Chinese J. Phys. 56 (1) (2018) 432–448.

[7] P. Rana, V. Makkar, G. Gupta, Finite element study of bio-convective Stefan blowing Ag-MgO/water hybrid nanofluid induced by stretching cylinder utilizing non-Fourier and non-Fick's laws, Nanomaterials 11 (7) (2021) 1735.

[8] H.A. Nabwey, S.I. Alshber, A.M. Rashad, A.E.N. Mahdy, Influence of bioconvection and chemical reaction on magneto—Carreau nanofluid flow through an inclined cylinder, Mathematics 10 (3) (2022) 504.

[9] S. Hussain, A.M. Aly, H.F. Öztop, Magneto-bioconvection flow of hybrid nanofluid in the presence of oxytactic bacteria in a lid-driven cavity with a streamlined obstacle, Int. Commun. Heat Mass Transfer 134 (2022) 106029.

[10] S.U. Choi, J.A. Eastman, Enhancing Thermal Conductivity of Fluids with Nanoparticles, Tech. Rep., Argonne National Lab.(ANL), Argonne, IL (United States), 1995.

[11] J. Buongiorno, Convective transport in nanofluids, J. Heat Transfer 128 (2006) 240–250.

[12] M. Hemmat Esfe, A.A. Abbasian Arani, M. Rezaie, W.-M. Yan, A. Karimipour, Experimental determination of thermal conductivity and dynamic viscosity of Ag–MgO/water hybrid nanofluid, Int. Commun. Heat Mass Transfer 66 (2015) 189–195.

[13] H. Sajjadi, A.A. Delouei, R. Mohebbi, M. Izadi, S. Succi, Natural convection heat transfer in a porous cavity with sinusoidal temperature distribution using Cu/water nanofluid: Double MRT lattice Boltzmann method, Commun. Comput. Phys. 29 (1) (2021) 292–318.

[14] F. Mebarek-Oudina, N. Keerthi Reddy, M. Sankar, Heat source location effects on buoyant convection of nanofluids in an annulus, in: Advances in Fluid Dynamics, Springer, 2021, pp. 923–937.

[15] A. Ahlawat, M.K. Sharma, Effects of heated block comprised porous stratum and micropolar hybrid nanofluid on convective heat transfer and entropy generation in a square enclosure, Heat Transf. 51 (6) (2022) 5320–5347.
[16] A.V. Kuznetsov, Nanofluid bioconvection in water-based suspensions containing nanoparticles and oxytactic microorganisms: oscillatory instability, Nanoscale Res. Lett. 6 (1) (2011) 1–13.
[17] O.A. Bég, V. Prasad, B. Vasu, Numerical study of mixed bioconvection in porous media saturated with nanofluid containing oxytactic microorganisms, J. Mech. Med. Biol. 13 (04) (2013) 1350067.
[18] K. Das, P.R. Duari, P.K. Kundu, Nanofluid bioconvection in presence of gyrotactic microorganisms and chemical reaction in a porous medium, J. Mech. Sci. Technol. 29 (11) (2015) 4841–4849.
[19] M.N. Tosin Oreyeni, P.A. Oladele, Triple stratification impacts on an inclined hydromagnetic bioconvective flow of micropolar nanofluid with exponential space-based heat generation, Waves Random Complex Media (2022) 1–23.
[20] M. Shamshuddin, S. Salawu, K. Ramesh, V.S. Patil, P. Humane, Bioconvective treatment for the reactive Casson hybrid nanofluid flow past an exponentially stretching sheet with Ohmic heating and mixed convection, J. Therm. Anal. Calorim. 148 (21) (2023) 12083–12095.
[21] M. Mastiani, M.M. Kim, A. Nematollahi, Density maximum effects on mixed convection in a square lid-driven enclosure filled with Cu-water nanofluids, Adv. Powder Technol. 28 (1) (2017) 197–214.
[22] B. Vasu, R.S.R. Gorla, O.A. Bég, P. Murthy, V. Prasad, A. Kadir, Unsteady flow of a nanofluid over a sphere with nonlinear Boussinesq approximation, J. Thermophys. Heat Transfer 33 (2) (2019) 343–355.
[23] M. Asmadi, R. Md Kasmani, Z. Siri, H. Saleh, Natural convection analysis of copper–alumina/water hybrid nanofluids in a U-shaped cavity with adiabatic wavy walls, Waves Random Complex Media (2022) 1–30.
[24] K. Ramesh, D. Kumar, M. Nazeer, D. Waqfi, F. Hussain, Mathematical modeling of MHD Jeffrey nanofluid in a microchannel incorporated with lubrication effects: a Graetz problem, Phys. Scr. 96 (2) (2020) 025225.
[25] S. Hussain, N. Alsedias, A.M. Aly, Natural convection of a water-based suspension containing nano-encapsulated phase change material in a porous grooved cavity, J. Energy Storage 51 (2022) 104589.
[26] A.M. Aly, A.-A. Hyder, N. Alsedias, Time-Conformable fractal systems of natural convection of tall fin inside two circular cylinders suspended by NEPCM, Alex. Eng. J. 61 (12) (2022) 12311–12328.
[27] A.M. Aly, N. Alsedias, A.M. Galal, The conformable fractal systems of natural convection in an annulus suspended by NEPCM, Int. Commun. Heat Mass Transfer 134 (2022) 106023.
[28] W. Alhejaili, A.M. Aly, Thermal radiation impacts on natural convection of NEPCM in a porous annulus between two horizontal wavy cavities, Case Stud. Therm. Eng. 40 (2022) 102526.
[29] S. Hussain, A.M. Aly, N. Alsedias, Bioconvection of oxytactic microorganisms with nano-encapsulated phase change materials in an omega-shaped porous enclosure, J. Energy Storage 56 (2022) 105872.
[30] S. Hussain, Z. Raizah, A.M. Aly, Thermal radiation impact on bioconvection flow of nano-enhanced phase change materials and oxytactic microorganisms inside a vertical wavy porous cavity, Int. Commun. Heat Mass Transfer 139 (2022) 106454.
[31] A. Alazzam, N.A. Qasem, A. Aissa, M.S. Abid, K. Guedri, O. Younis, Natural convection characteristics of nano-encapsulated phase change materials in a rectangular wavy enclosure with heating element and under an external magnetic field, J. Energy Storage 57 (2023) 106213.
[32] S. Hussain, M. Molana, T. Armaghani, A. Rashad, H.A. Nabwey, Energy storage performance and irreversibility analysis of a water-based suspension containing nano-encapsulated phase change materials in a porous staggered cavity, J. Energy Storage 53 (2022) 104975.
[33] S. Hussain, P. Jayavel, B. Almutairi, K. Ramesh, Investigation of MHD oxytactic microorganisms with NEPCMs in rectotrapezoidal enclosure with FEM: Applications to energy storage technologies, J. Magn. Magn. Mater. 592 (2024) 171808.
[34] S. Hussain, F. Ertam, M.B.B. Hamida, H.F. Oztop, N.H. Abu-Hamdeh, Analysis of bioconvection and oxytactic microorganisms in a porous cavity with nano-enhanced phase change materials and quadrant heater: Application of support vector regression based model, J. Energy Storage 63 (2023) 107059.
[35] S. Hussain, F. Schieweck, S. Turek, Efficient Newton-multigrid solution techniques for higher order space–time Galerkin discretizations of incompressible flow, Appl. Numer. Math. 83 (2014) 51–71.
[36] S. Hussain, K. Mehmood, M. Sagheer, A. Farooq, Entropy generation analysis of mixed convective flow in an inclined channel with cavity with Al_2O_3-water nanofluid in porous medium, Int. Commun. Heat Mass Transfer 89 (2017) 198–210.
[37] S. Hussain, S. Shoeibi, T. Armaghani, Impact of magnetic field and entropy generation of casson fluid on double diffusive natural convection in staggered cavity, Int. Commun. Heat Mass Transfer 127 (2021) 105520.
[38] B. Ghasemi, S. Aminossadati, A. Raisi, Magnetic field effect on natural convection in a nanofluid-filled square enclosure, Int. J. Therm. Sci. 50 (9) (2011) 1748–1756.
[39] A.B. Çolak, An experimental study on the comparative analysis of the effect of the number of data on the error rates of artificial neural networks, Int. J. Energy Res. 45 (1) (2021) 478–500.
[40] A.B. Çolak, A new study on the prediction of the effects of road gradient and coolant flow on electric vehicle battery power electronics components using machine learning approach, J. Energy Storage 70 (2023) 108101.
[41] A.B. Çolak, O. Acikgoz, Y. Karakoyun, A. Koca, A.S. Dalkilic, Experimental and numerical investigations on the heat transfer characteristics of a real-sized radiant cooled wall system supported by machine learning, Int. J. Therm. Sci. 191 (2023) 108355.
[42] T. Güzel, A.B. Çolak, Performance prediction of current-voltage characteristics of schottky diodes at low temperatures using artificial intelligence, Microelectron. Reliab. 147 (2023) 115040.